

# Quantum Computer-Based Verification of Quantum Thermodynamic Uncertainty Relation

Nobumasa Ishida\* and Yoshihiko Hasegawa†

Department of Information and Communication Engineering,  
Graduate School of Information Science and Technology,  
The University of Tokyo, Tokyo 113-8656, Japan

Quantum thermodynamic uncertainty relations establish the fundamental trade-off between precision and thermodynamic costs, yet their empirical verification is scarce. To extend the range of real-world tests, we present an approach that utilizes a noisy quantum computer for verifying a general quantum thermodynamic uncertainty relation. We employ a three-fold methodology to tackle the limitations of current quantum processors: generalizing a thermodynamic uncertainty relation to arbitrary observables under completely positive trace-preserving maps, proposing a method to measure the thermodynamic cost (survival activity) in the weak coupling regime, and reducing the required circuit depth by exploiting the properties of our thermodynamic uncertainty relation. We apply our bound to a quantum time correlator measurement protocol on IBM's cloud-based quantum processor. The empirical results show that our bound tightly constrains precision, with the relative variance approaching the theoretical limit within a single order of magnitude. Furthermore, our approach enables the saturation of our thermodynamic uncertainty relation by constructing the optimal observable that requires entangled measurements. This study highlights the potential and limitations of noisy quantum computers for demonstrating quantum thermodynamic trade-offs.

*Introduction.*—Thermodynamics constrains the quality of information processing. Recent progress in quantum thermodynamics has revealed trade-off relations between the performance of quantum systems and physical costs [1–7]. Among these, quantum thermodynamic uncertainty relations (TURs) have emerged as significant achievements, elucidating trade-offs between the precision of observables and thermodynamic costs, such as entropy production and dynamical activity [7–22]. The quantum TURs are expected to be fundamental relations that hold for diverse systems and represent trade-offs beyond precision [23–25]. However, despite theoretical advances, empirical verification is limited to a few studies [26–28]. Addressing this challenge is necessary to establish the practically relevant relations that can serve as tight constraints on real devices.

In this Letter, we propose using a noisy quantum computer to verify a general quantum TUR that has not been validated empirically. While quantum computers are promising as versatile testbeds for quantum physics [29–33], current processors face limitations on the executable quantum circuit depth due to low gate fidelity and short coherence time [34–36]. To maximize the limited capabilities, we employ three key strategies. First, we derive a quantum TUR that bounds any observable under the general quantum processes described by completely positive trace-preserving (CPTP) maps, ensuring applicability to the noisy quantum channels of quantum computers. Second, we introduce a method to measure the thermodynamic cost in our bound—survival activity [19]—in the weak coupling regime using the Neumann series. Third, by exploiting the properties of quantities entering the general TUR, we reduce controlled unitary operations in our circuits, thereby lowering the circuit

depth. Using IBM's cloud-based quantum processor [37], we apply the general TUR to a protocol for measuring quantum time correlators as a representative example. The empirical results show that our bound imposes a tight constraint on the precision, with the variation, or relative variance, reaching values as low as a few dozen times the thermodynamic limit. Furthermore, we achieve equality in our TUR using optimal observables that require entangled measurements. This study suggests the potential and limitations of near-term noisy processors in exploring thermodynamic trade-offs on actual quantum systems.

*Results.*—We derive a quantum TUR applicable to arbitrary observables under any CPTP maps, which are the most general descriptions of quantum processes. Such a general TUR is not only theoretically important for its generality but also necessary to bound observables on quantum computers evolving under noisy quantum channels [38]. Consider a generic quantum system  $S$  and an environment  $E$ , illustrated in Fig. 1a. Initially, at time  $t = 0$ , the systems  $S$  and  $E$  are independent. The composite system  $S+E$  evolves under the unitary dynamics  $U_{SE}$  until  $t = T$ , representing a CPTP map  $\Phi$  on the principal system  $S$ . We denote the initial state of  $S$  by  $|\Psi_S(0)\rangle$  or  $\rho_S(0)$  and that of  $E$  by  $|0_E\rangle$ . Although the following theoretical results remain valid even if  $\rho_S(0)$  is mixed [39], we assume  $\rho_S(0)$  is pure to simplify the notation. The final state of  $S+E$  is  $|\Psi_{SE}(T)\rangle = U_{SE}(|\Psi_S(0)\rangle \otimes |0_E\rangle)$ . By choosing an orthonormal basis  $\{|\phi_m\rangle\}$  for  $E$ , we can express  $|\Psi_{SE}(T)\rangle$  as  $\sum_m V_m |\Psi_S(0)\rangle \otimes |\phi_m\rangle$ , where  $V_m$  is a Kraus operator defined by  $V_m = \langle \phi_m | U_{SE} | 0_E \rangle$ . These operators satisfy the completeness relation  $\sum_m V_m^\dagger V_m = I_S$ , where  $I_S$  is the identity operator. The final state of  $S$  is

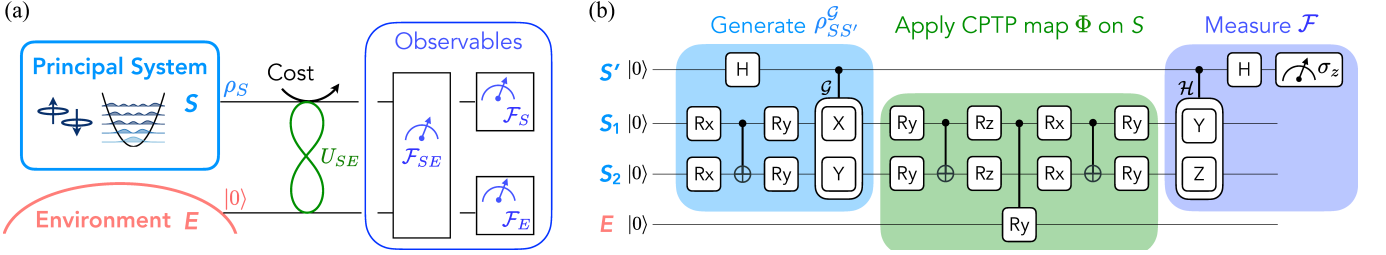


FIG. 1. Illustration of the general quantum system composed of a principal system  $S$  and the environment  $E$ . System  $S$  interacts with  $E$  under the unitary dynamics  $U_{SE}$  on  $S+E$ , yielding a CPTP map  $\Phi$  on  $S$  as a reduced dynamics. Our focus is on the expectation value and variance of generic observables  $\mathcal{F}$ , including local observables on  $S$  or  $E$ , for the final state of  $S+E$ . (b) Quantum circuit for measuring the quantum time correlator  $\text{Re}[R(T)]$ , where the general TUR is verified. We take  $\mathcal{G} = \sigma_x \otimes \sigma_y$  and  $\mathcal{H} = \sigma_y \otimes \sigma_z$  as examples. We randomly choose  $\mathcal{G}$  and  $\mathcal{H}$  as tensor products of Pauli or identity operators, except for  $I \otimes I$ . Rotation gates, including ones for preparing the initial state of  $S$ , are also randomly parameterized. The rotation angle of the controlled RY gate between  $S$  and  $E$  is given by  $\pi\gamma/2$  with  $\gamma$  being interaction strength. The shaded sections of the circuit correspond to their respective colored segments in (a).

$$\rho_S(T) = \Phi(\rho_S(0)) = \sum_m V_m \rho_S(0) V_m^\dagger, \text{ obtained by tracing out } E \text{ from } |\Psi_{SE}(T)\rangle.$$

We aim to characterize the fluctuation of observables represented by a Hermitian operator  $\mathcal{F}$  on the composite system  $S+E$  at the final time. The target observable  $\mathcal{F}$  is generic; it can be a global observable that spans  $S+E$  with entangled eigenbases, a separable observable whose eigenbases are separable between  $S$  and  $E$ , an independent observable of the form  $\mathcal{F}_S \otimes \mathcal{F}_E$ , or a local observable given by either  $\mathcal{F}_S \otimes I_E$  or  $I_S \otimes \mathcal{F}_E$ . We define the expectation value of  $\mathcal{F}$  as  $\langle \mathcal{F} \rangle = \langle \Psi_{SE}(T) | \mathcal{F} | \Psi_{SE}(T) \rangle$ , and its variance as  $\text{Var}[\mathcal{F}] = \langle \mathcal{F}^2 \rangle - \langle \mathcal{F} \rangle^2$ . We show the following TUR bounding the precision of arbitrary observable  $\mathcal{F}$ :

$$\frac{\text{Var}[\mathcal{F}]}{(\langle \mathcal{F} \rangle - \mathcal{C}_\mathcal{F})^2} \geq \frac{1}{\mathcal{A}}, \quad (1)$$

where  $\mathcal{A} = \text{Tr}[\rho_S(0)(V_0^\dagger V_0)^{-1}] - 1$  is a thermodynamic cost called survival activity [19], and  $\mathcal{C}_\mathcal{F}$  represents inherent-dynamics contribution defined by  $\mathcal{C}_\mathcal{F} = \text{Re}[\langle \tilde{\Psi}_{SE}(0) | \mathcal{F} | \Psi_{SE}(T) \rangle]$  with the unnormalized state  $|\tilde{\Psi}_{SE}(0)\rangle = (V_0^{-1})^\dagger |\Psi_S(0)\rangle \otimes |\phi_0\rangle$ . Equality is achieved when  $\rho_S(0)$  is pure and  $\mathcal{F}$  is proportional to an observable  $\mathcal{L} = |\Psi_{SE}(T)\rangle \langle \Psi_{SE}(T)| - 1/2(|\tilde{\Psi}_{SE}(0)\rangle \langle \Psi_{SE}(T)| + |\Psi_{SE}(T)\rangle \langle \tilde{\Psi}_{SE}(0)|)$ .

Equation (1) is hereafter referred to as the general TUR. It states that the high precision of observables, characterized by relative fluctuations, requires a correspondingly high thermodynamic cost quantified by the survival activity  $\mathcal{A} (\geq 0)$ . The general TUR is distinguished by three primary characteristics; it is (i) applicable to any observables on  $S+E$ , (ii) valid for any initial state of  $S$  and any CPTP dynamics on  $S$  as long as  $V_0^{-1}$  is defined, and (iii) tight in the sense that equality is achievable. The general TUR is derived based on the quantum Cramér–Rao inequality from quantum estimation theory [46–49], accounting for the estimation of a virtual perturbation on the CPTP map. We defer the derivation to the manuscript’s conclusion.

The survival activity  $\mathcal{A}$  quantifies the intensity of the interaction between  $S$  and  $E$ . In the context of Markovian open quantum systems,  $\mathcal{A}$  is associated with dynamical activity, which counts the number of jumps [19]. The inherent-dynamics contribution  $\mathcal{C}_\mathcal{F}$  measures the influence of unitary dynamics on  $S$ . To clarify this, consider a local observable  $\mathcal{F}_S$  on  $S$  in the weak coupling regime between  $S$  and  $E$ . In this regime,  $V_0$  is nearly unitary, which can be expressed as  $V_0^\dagger V_0 = I_S - \epsilon$  with  $\epsilon$  an operator of small norm. Using the polar decomposition  $V_0 = U_0 \sqrt{V_0^\dagger V_0}$ , we can approximate  $\mathcal{C}_{\mathcal{F}_S}$  as  $\mathcal{C}_{\mathcal{F}_S} \approx \langle \Psi_S(0) | V_0^\dagger F_S V_0 | \Psi_S(0) \rangle + \text{Re}[\langle \Psi_S(0) | \epsilon U_0^\dagger F_S U_0 | \Psi_S(0) \rangle]$ . The primary term of  $\mathcal{C}_{\mathcal{F}_S}$  represents the expectation of  $F_S$  in the absence of jumps on  $E$  (under the condition of  $|\phi_0\rangle = |0_E\rangle$ ) [50]. We note that for special local observables on  $E$  called counting observables,  $\mathcal{C}_\mathcal{F}$  vanishes and the previous TUR [19] is recovered [39].

We show the way to measure the survival activity  $\mathcal{A}$  and the inherent-dynamics contribution  $\mathcal{C}_\mathcal{F}$ . These quantities include a term  $V_0^{-1}$ , which is intractable due to the difficulty in directly inverting an operator. The Neumann series expansion of  $(V_0^\dagger V_0)^{-1}$  can be utilized to circumvent this challenge. This allows the inverse to be expressed in terms of a series of accessible expectation values, effectively removing the need for direct operator inversion. As a result,  $\mathcal{A}$  is expanded as  $\mathcal{A} = \lim_{N \rightarrow \infty} \sum_{n=0}^N (-1)^n \binom{N+1}{n+1} \text{Tr}[\rho_S(0)(V_0^\dagger V_0)^n] - 1$ , where the expectations  $\text{Tr}[\rho_S(0)(V_0^\dagger V_0)^n]$  can be feasibly estimated. When the interaction between  $S$  and  $E$  is weak, we can approximate  $\mathcal{A}$  by truncating the series [39]. In the following, we set  $N = 1$  and obtain  $\mathcal{A} \approx 1 - p_0$ , where  $p_0 = \text{Tr}[\rho_S(0)V_0^\dagger V_0]$  represents the probability of no environmental jumps occurring.  $\mathcal{C}_\mathcal{F}$  is similarly approximated as  $\mathcal{C}_\mathcal{F} \approx 2C_1 - C_2$ , where  $C_1 = \text{Re}[\langle \Psi_S(0) | \otimes \langle \phi_0 | (V_0^\dagger \otimes I_E) \mathcal{F} U_{SE} | \Psi_{SE}(0) \rangle]$  and  $C_2 = \text{Re}[\langle \Psi_S(0) | \otimes \langle \phi_0 | (V_0^\dagger V_0 V_0^\dagger \otimes I_E) \mathcal{F} U_{SE} | \Psi_{SE}(0) \rangle]$ , which are the correlators of operators.

Measuring the correlators  $C_1$  and  $C_2$  is particu-

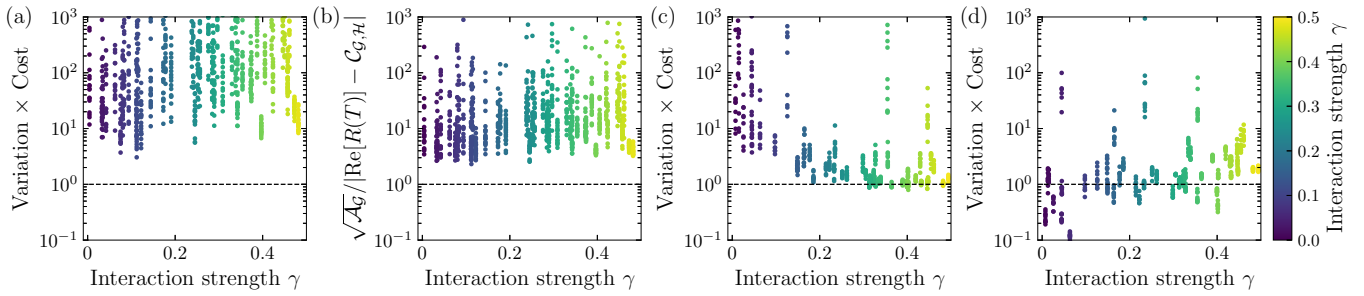


FIG. 2. Demonstration of the general TUR and its equality condition on IBM’s quantum processor (ibm\_torino). For each plot, the dashed line represents the theoretical limit given by unity, and the point colors indicate the interaction strength  $\gamma$  between the principal system  $S$  and the environment  $E$ . (a) Validation of the general TUR for the observable  $\mathcal{F}_{\text{corr}}$  regarding the quantum time correlator  $R(T)$ . The product of the variation  $\text{Var}[\mathcal{F}_{\text{corr}}]/(\langle \mathcal{F}_{\text{corr}} \rangle - \mathcal{C}_{\mathcal{F}_{\text{corr}}})^2$  and the thermodynamic cost (survival activity)  $\mathcal{A}_G$  is plotted against  $\gamma$ . (b) Validation of the thermodynamic bound on the evolution of  $R(T)$ . The ratio between  $\sqrt{\mathcal{A}_G}$  and the difference  $|\text{Re}[R(T)] - \mathcal{C}_{G,H}|$  is plotted against  $\gamma$ . The data used are the same as in (a). (c) Validation of the equality condition of the general TUR. The product of the variation of  $\mathcal{F}_{\text{opt}}$  and the cost is plotted against  $\gamma$ . (d) Results for  $\mathcal{F}_{\text{opt}}$  obtained using a straightforward implementation of the circuits for  $\mathcal{C}_{\mathcal{F}_{\text{opt}}}$ . Settings: For (a) and (b), 50 circuits with different parameters were constructed, each undergoing 4,000 measurements, repeated 20 times. For (c) and (d), 50 circuits were also constructed, but with 8,000 measurements each, repeated 10 times, and (d) used the same parameters as (c).

larly challenging. These correlators are measured using Hadamard tests [51], which require an ancilla qubit prepared in  $|+\rangle = \frac{1}{\sqrt{2}}(|0\rangle + |1\rangle)$ . A straightforward implementation of the test for measuring  $C_1$  involves sequentially applying controlled versions of  $U_{SE}$ ,  $\mathcal{F}_i$ , and  $V_0$ , with the ancilla  $S'$  serving as the control qubit, followed by a measurement of  $S'$ . Here,  $\mathcal{F}_i$  is some unitary decomposition of  $\mathcal{F}$  satisfying  $\sum_i \mathcal{F}_i = \mathcal{F}$ . Measuring  $C_2$  requires the application of additional controlled unitary operations. However, this straightforward protocol results in circuits that are too deep to be executed accurately on current processors, as controlled unitary operations involving multiple qubits are demanding in practice. To address this challenge, we reduce the depth of the circuits for  $C_1$  and  $C_2$  in the following two demonstrations by exploiting the structure of the operators in the correlators. Notably, the *physical circuits* implemented on the hardware are often much longer than the corresponding *logical circuits* due to physical constraints such as qubit connectivity and the limited set of native gates, which necessitates gate decomposition [52].

We conduct two demonstrations on IBM’s superconducting quantum processor “Heron” (ibm\_torino) [37]. The processor’s characteristics, such as coherence time and error rates, are provided in Ref. [39]. First, we apply the general TUR to a protocol for measuring quantum time correlators, revealing the cost-precision trade-off on quantum circuits. Second, we validate the equality condition of the general TUR by constructing the optimal observable. In both demonstrations, we carefully consider the depth of quantum circuits (i.e., the number of sequentially executed gates) to ensure accurate results on the current processor.

We first focus on the initial demonstration. We consider the two-point time correlator  $R(t) =$

$\langle \mathcal{H}(t)\mathcal{G} \rangle_{\rho_{S(0)}} = \text{Tr}[\rho_{S(0)}\mathcal{H}(t)\mathcal{G}]$  of unitary observables  $\mathcal{G}$  and  $\mathcal{H}$ , where  $\mathcal{H}(t) = \sum_m V_m^\dagger \mathcal{H} V_m$  is the Heisenberg picture of  $\mathcal{H}$  at time  $t$ . The quantity  $R(T)$  characterizes the evolution of spin and fermionic systems [53–56]. Figure 1b illustrates the main circuit, which is used for measuring  $R(T)$ . Based on Ref. [57], this circuit employs an Hadamard test with an ancilla qubit  $S'$  [51]. The principal system  $S$ , consisting of two qubits modeling spins under environmental noise, is entangled with  $S'$  through a controlled unitary operation  $U_G^{(c)}$  that applies  $\mathcal{G}$  to  $S$  conditioned on  $S'$ . System  $S$  then undergoes a CPTP map  $\Phi$  followed by  $U_H^{(c)}$ , with  $U_{SE}$  for  $\Phi$  characterized by the interaction strength  $\gamma$  between  $S$  and the environment  $E$ . The real part of  $R(T)$  is determined by measuring Pauli operator  $\sigma_x$  on  $S'$  at the final time. The general TUR holds for this setup with the observable  $\mathcal{F}_{\text{corr}} = U_H^{(c)\dagger}(\sigma_x \otimes I_S)U_H^{(c)}$  satisfying  $\langle \mathcal{F}_{\text{corr}} \rangle = \text{Re}[R(T)]$  and the initial state  $\rho_{S'S}^G = U_G^{(c)}(|+\rangle\langle+| \otimes \rho_S(0))U_G^{(c)\dagger}$ . The survival activity  $\mathcal{A}_G$  is defined for the state  $\rho_{S'S}^G$ . Crucially, the inherent-dynamics contribution  $\mathcal{C}_{\mathcal{F}_{\text{corr}}} = \text{Re}[\text{Tr}[\rho_{S'S}^G(I_{S'} \otimes V_0^{-1})\mathcal{F}_{\text{corr}}(I_{S'} \otimes V_0)]]$  depends only on  $V_0$  from the set  $\{V_k\}$  constructing  $U_{SE}$ . This enables a reduction in the number of controlled unitary operations required for measuring  $C_1$  and  $C_2$ . Consequently, quantum circuit depth is reduced to one-tenth of the straightforward implementation (median depths for  $C_1$ : 592.5  $\rightarrow$  61,  $C_2$ : 1056  $\rightarrow$  95) [39].

Figure 2a shows the results on the general TUR for the circuit measuring the time correlators. We find that the empirical values of the product of the variation of  $\mathcal{F}_{\text{corr}}$  given by  $\text{Var}[\mathcal{F}_{\text{corr}}]/(\langle \mathcal{F}_{\text{corr}} \rangle - \mathcal{C}_{\mathcal{F}_{\text{corr}}})^2$  and the survival activity  $\mathcal{A}_G$  exceed 1, as predicted by the general TUR in Eq. (1). Although our circuit was not designed to minimize variation, our results show that the empir-

ical variation approaches the theoretical limit within a single order of magnitude, suggesting that survival activity effectively constrains the precision of observables on current devices. We discuss the effectiveness of circuit optimization and errors in Ref. [39].

Beyond the trade-off concerning precision, we can derive a specific thermodynamic bound on the quantum time correlator  $R(T)$  based on the general TUR as follows:

$$|\text{Re}[R(T)] - \mathcal{C}_{\mathcal{G}, \mathcal{H}}| \leq \sqrt{\mathcal{A}_{\mathcal{G}}}, \quad (2)$$

where the inherent-dynamics contribution  $\mathcal{C}_{\mathcal{G}, \mathcal{H}}$  for the time correlator, equivalent to  $\mathcal{C}_{\mathcal{F}_{\text{corr}}}$ , reads  $\mathcal{C}_{\mathcal{G}, \mathcal{H}} = \text{Re}[\text{Tr}[\rho_S(0)(V_0^{-1}\mathcal{H}V_0\mathcal{G} + \mathcal{G}V_0^{-1}\mathcal{H}V_0)]]/2$ . Equation (2) states that the thermodynamic cost bounds the deviation of the time correlator  $R(T)$  from the correlation caused by the inherent dynamics on  $S$ . In the weak coupling regime where  $V_0^\dagger V_0 = I_S - \epsilon$ ,  $\mathcal{C}_{\mathcal{G}, \mathcal{H}}$  is approximated as  $\mathcal{C}_{\mathcal{G}, \mathcal{H}} \approx \text{Re}[\langle V_0^\dagger \mathcal{H}V_0 \mathcal{G} \rangle_{\rho_S(0)}] + \text{Re}[\langle \epsilon U_0^\dagger \mathcal{H}U_0 \mathcal{G} \rangle_{\rho_S(0)} + \langle \mathcal{G} U_0^\dagger \mathcal{H}U_0 \rangle_{\rho_S(0)}]/2$  with  $U_0$  defined above. The primary term represents the time correlator between  $\mathcal{G}$  and  $\mathcal{H}$  under the inherent dynamics on  $S$  described by  $V_0$ . In Fig. 2b, we show the results for the bound of  $\text{Re}[R(T)]$  in Eq. (2) using the same set of outcomes in Fig. 2a. We find that all empirical values adhere to the theoretical bound. The figure of merit, given by the ratio  $\sqrt{\mathcal{A}_{\mathcal{G}}}/|\text{Re}[R(T)] - \mathcal{C}_{\mathcal{G}, \mathcal{H}}|$ , approaches the limit within a small constant factor, suggesting the empirical tightness of the bound.

Next, we explore the optimal observable  $\mathcal{F}_{\text{opt}} = \mathcal{L}$ , which saturates the general TUR in Eq. (1). Measuring  $\mathcal{F}_{\text{opt}}$  typically requires entangled measurements across  $S$  and  $E$ , making it challenging to implement. However, quantum computers offer the versatility to construct the necessary unitary operation, making  $\mathcal{F}_{\text{opt}}$  tractable. For a two-qubit system with one qubit each for  $S$  and  $E$ , we theoretically obtain  $\mathcal{F}_{\text{opt}}$  given  $U_{SE}$  and diagonalize it as  $\mathcal{F}_{\text{opt}} = U_{\mathcal{F}_{\text{opt}}}^\dagger \Lambda U_{\mathcal{F}_{\text{opt}}}$ . By implementing the unitary dynamics  $U_{\mathcal{F}_{\text{opt}}}$  on  $S+E$ , we can access  $\mathcal{F}_{\text{opt}}$  through the Heisenberg picture of the diagonal operator  $\Lambda$ , which is measurable. Remarkably, any two-qubit unitary dynamics can be realized using three CNOT gates and several one-qubit gates [58], making this approach feasible on quantum computers. The difficulty lies in measuring  $C_1$  and  $C_2$  for  $\mathcal{F}_{\text{opt}}$ , because they require lengthy circuits for Hadamard tests. We reduce the circuit depth by decomposing complex controlled unitary operations into a combination of original unitary operations and Toffoli (controlled-CNOT) gates [39]. Furthermore, this design allows for the use of approximate Toffoli gates [59], which sacrifice exact operation in favor of simplified implementation, without compromising overall accuracy in our circuit. Consequently, the depth is reduced by an order of magnitude compared to the straightforward implementation (median depths for  $C_1$ : 539  $\rightarrow$  48.5,  $C_2$ : 720  $\rightarrow$  90).

Figure 2c shows the results for  $\mathcal{F}_{\text{opt}}$ . The observed data points closely approach the theoretical limit, except for the small interaction strength  $\gamma$ . We attribute the discrepancies at small  $\gamma$  to the readout error in measuring  $\mathcal{A}$  (around  $2.0 \times 10^{-2}$ ) [39]. Despite these deviations, the results demonstrate that the general TUR can be saturated by the optimal observable  $\mathcal{F}_{\text{opt}}$ , highlighting the potential of quantum computer-based verification. In contrast, Fig. 2d shows the results for the nonoptimized circuits, which violate the bound. This emphasizes the necessity of our method for reducing circuit depth. Furthermore, we compared the results obtained from the optimized circuits on the Heron processor with those from the previous-generation “Eagle” processor [33, 37, 41], which underlines the importance of the Heron processor’s accuracy for our demonstrations [39].

*Discussion.*—We have demonstrated a quantum TUR using a noisy quantum computer. Our study stands out from previous works that used quantum computers to verify fluctuation theorems [60–62] by focusing on the tightness of our relation. Investigating tightness is crucial for quantum TURs; merely confirming the general TUR on systems where empirical values are far from the thermodynamic limit does not establish the bound as a fundamental trade-off relation relevant in real devices. We have validated the tightness of the general TUR on a quantum circuit for a practical protocol, uncovering the potential of near-term quantum processors in exploring such trade-off relations. Our work also reveals the limitations of current processors, necessitating circuit optimization to enhance result accuracy. This study opens a new avenue for utilizing emerging quantum computers to verify quantum thermodynamic trade-offs on actual quantum systems.

*Derivation.*—We present the derivation of the general TUR in Eq. (1). See Ref. [39] for the details. We utilize the quantum Cramér–Rao inequality from quantum estimation theory [46–49], which provides a lower bound on the variance of estimators. We consider the estimation problem of a parameter  $\theta$ , which virtually perturbs the CPTP map. The virtual perturbation is introduced by the following Kraus operators on  $S$  as in Ref. [19]:  $V_m(\theta) = e^{\theta/2} V_m$  for  $m \geq 1$  and  $V_0(\theta) = U_0 \sqrt{I - e^\theta \sum_{m \geq 1}^M V_m^\dagger V_m}$ , where  $U_0$  is a unitary operator in the polar decomposition  $V_0 = U_0 \sqrt{V_0^\dagger V_0}$ . The original dynamics is recovered when  $\theta = 0$ . For any observables  $\mathcal{F}$  on  $S+E$ , the quantum Cramér–Rao inequality states  $\text{Var}[\mathcal{F}]/(\partial_\theta \langle \mathcal{F} \rangle_{\theta=0})^2 \geq 1/J$ , where  $J$  is the quantum Fisher information [48, 49, 63]. The scaling of the expectation of the observable  $\mathcal{F}$  regarding  $\theta$  is given by  $\partial_\theta \langle \mathcal{F} \rangle_\theta = \partial_\theta \langle \Psi_{SE}(T)_\theta | \mathcal{F} | \Psi_{SE}(T)_\theta \rangle = (\sum_k \langle \Psi_S(0) | dV_k(\theta)^\dagger / d\theta \otimes |\phi_k\rangle) \mathcal{F} (\sum_l V_l(\theta) | \Psi_S(0) \rangle \otimes |\phi_l\rangle) + \text{h.c.}$ . We can calculate the derivative of  $V_0$  as  $dV_0(\theta)/d\theta = 1/2(V_0 - (V_0^{-1})^\dagger)$ . Using this result, we obtain  $\partial_\theta \langle \mathcal{F} \rangle_{\theta=0} = \langle \mathcal{F} \rangle - \mathcal{C}_{\mathcal{F}}$ .  $J$  is calculated as in

Ref. [19] and we obtain  $J = \mathcal{A}$ . Combining these results, we obtain the general TUR in Eq. (1). The equality condition of the general TUR comes from that of the quantum Cramér–Rao inequality, where equality is achieved by the symmetric logarithmic derivative  $\mathcal{L}$  [47].

This work was supported by JSPS KAKENHI Grant Numbers JP23KJ0576 and JP23K24915.

certainty relation for continuous measurement, *Phys. Rev. Lett.* **125**, 050601 (2020).

- [16] H. J. D. Miller, M. H. Mohammady, M. Perarnau-Llobet, and G. Guarnieri, Thermodynamic uncertainty relation in slowly driven quantum heat engines, *Phys. Rev. Lett.* **126**, 210603 (2021).
- [17] J. Liu and D. Segal, Coherences and the thermodynamic uncertainty relation: insights from quantum absorption refrigerators, *Phys. Rev. E* **103**, 032138 (2021).
- [18] A. A. S. Kalaee, A. Wacker, and P. P. Potts, Violating the thermodynamic uncertainty relation in the three-level maser, *Phys. Rev. E* **104**, L012103 (2021).
- [19] Y. Hasegawa, Thermodynamic uncertainty relation for general open quantum systems, *Phys. Rev. Lett.* **126**, 010602 (2021).
- [20] Y. Hasegawa, Thermodynamic uncertainty relation for quantum first-passage processes, *Phys. Rev. E* **105**, 044127 (2022).
- [21] T. Van Vu and K. Saito, Thermodynamics of precision in Markovian open quantum dynamics, *Phys. Rev. Lett.* **128**, 140602 (2022).
- [22] T. Monnai, Thermodynamic uncertainty relation for quantum work distribution: exact case study for a perturbed oscillator, *Phys. Rev. E* **105**, 034115 (2022).
- [23] P. Pietzonka and U. Seifert, Universal trade-off between power, efficiency, and constancy in steady-state heat engines, *Phys. Rev. Lett.* **120**, 190602 (2018).
- [24] V. Van Tuan, T. Van Vu, and Y. Hasegawa, Unified thermodynamic–kinetic uncertainty relation, *J. Phys. A: Math. Theor.* **55**, 405004 (2022).
- [25] G. Falasco, M. Esposito, and J.-C. Delvenne, Beyond thermodynamic uncertainty relations: nonlinear response, error-dissipation trade-offs, and speed limits, *J. Phys. A: Math. Theor.* **55**, 124002 (2022).
- [26] H. M. Friedman, B. K. Agarwalla, O. Shein-Lumbroso, O. Tal, and D. Segal, Thermodynamic uncertainty relation in atomic-scale quantum conductors, *Phys. Rev. B* **101**, 195423 (2020).
- [27] S. Pal, S. Saryal, D. Segal, T. S. Mahesh, and B. K. Agarwalla, Experimental study of the thermodynamic uncertainty relation, *Phys. Rev. Res.* **2**, 022044 (2020).
- [28] X. He, P. Pakkiam, A. A. Gangat, M. J. Kewming, G. J. Milburn, and A. Fedorov, Effect of measurement back-action on quantum clock precision studied with a superconducting circuit, *Phys. Rev. Appl.* **20**, 034038 (2023).
- [29] G. García-Pérez, M. A. C. Rossi, and S. Maniscalco, IBM Q Experience as a versatile experimental testbed for simulating open quantum systems, *npj Quantum Information* **6**, 1 (2020).
- [30] G. Gustafson, S. Prestel, M. Spannowsky, and S. Williams, Collider events on a quantum computer, *J. High Energy Phys.* **2022**, 35.
- [31] P. T. Dumitrescu, J. G. Bohnet, J. P. Gaebler, A. Hankin, D. Hayes, A. Kumar, B. Neyenhuis, R. Vasseur, and A. C. Potter, Dynamical topological phase realized in a trapped-ion quantum simulator, *Nature* **607**, 463 (2022).
- [32] L. O. Conlon, T. Vogl, C. D. Marciak, I. Pogorelov, S. K. Yung, F. Eilenberger, D. W. Berry, F. S. Santana, R. Blatt, T. Monz, P. K. Lam, and S. M. Assad, Approaching optimal entangling collective measurements on quantum computing platforms, *Nat. Phys.* **19**, 351 (2023).
- [33] Y. Kim, A. Eddins, S. Anand, K. X. Wei, E. van den Berg, S. Rosenblatt, H. Nayfeh, Y. Wu, M. Zalevsky, and Y. Hasegawa, Quantum thermodynamic uncertainty relation for continuous measurement, *Phys. Rev. Lett.* **125**, 050601 (2020).

\* ishida@biom.t.u-tokyo.ac.jp

† hasegawa@biom.t.u-tokyo.ac.jp

tel, K. Temme, and A. Kandala, Evidence for the utility of quantum computing before fault tolerance, *Nature* **618**, 500 (2023).

[34] J. Preskill, Quantum computing in the NISQ era and beyond, *Quantum* **2**, 79 (2018).

[35] Y. Zhou, E. M. Stoudenmire, and X. Waintal, What limits the simulation of quantum computers?, *Phys. Rev. X* **10**, 041038 (2020).

[36] B. Cheng, X.-H. Deng, X. Gu, Y. He, G. Hu, P. Huang, J. Li, B.-C. Lin, D. Lu, Y. Lu, C. Qiu, H. Wang, T. Xin, S. Yu, M.-H. Yung, J. Zeng, S. Zhang, Y. Zhong, X. Peng, F. Nori, and D. Yu, Noisy intermediate-scale quantum computers, *Front. Phys.* **18**, 21308 (2023).

[37] IBM, IBM Quantum, <https://quantum.ibm.com/>, accessed: 2024-4-25.

[38] M. A. Nielsen and I. L. Chuang, *Quantum Computation and Quantum Information: 10th Anniversary Edition* (Cambridge University Press, 2010).

[39] See Supplemental Material for details, which includes Refs. [40–45].

[40] IBM, IBM debuts next-generation quantum processor & IBM Quantum System Two, extends roadmap to advance era of quantum utility, <https://newsroom.ibm.com/2023-12-04-IBM-Debuts-Next-Generation-Quantum-Processor-IBM-Quantum-System-Two,-Extends-Roadmap-to-Advance-Era-of-Quantum-Utility>, accessed: 2024-4-29.

[41] D. C. McKay, I. Hincks, E. J. Pritchett, M. Carroll, L. C. G. Govia, and S. T. Merkel, Benchmarking quantum processor performance at scale, [arXiv:2311.05933](https://arxiv.org/abs/2311.05933) (2023).

[42] J. Koch, T. M. Yu, J. Gambetta, A. A. Houck, D. I. Schuster, J. Majer, A. Blais, M. H. Devoret, S. M. Girvin, and R. J. Schoelkopf, Charge-insensitive qubit design derived from the Cooper pair box, *Phys. Rev. A* **76**, 042319 (2007).

[43] IBM, IBM Quantum breaks the 100-qubit processor barrier, <https://www.ibm.com/quantum/blog/127-qubit-quantum-processor-eagle>, accessed: 2024-2-24.

[44] N. Sundaresan, I. Lauer, E. Pritchett, E. Magesan, P. Jurcevic, and J. M. Gambetta, Reducing unitary and spectator errors in cross resonance with optimized rotary echoes, *PRX Quantum* **1**, 020318 (2020).

[45] Qiskit contributors, Qiskit, <https://github.com/QISKit>, accessed: 2024-6-2.

[46] C. W. Helstrom, Quantum detection and estimation theory, *J. Stat. Phys.* **1**, 231 (1969).

[47] M. Hotta and M. Ozawa, Quantum estimation by local observables, *Phys. Rev. A* **70**, 022327 (2004).

[48] M. G. A. Paris, Quantum estimation for quantum technology, *Int. J. Quantum Inform.* **07**, 125 (2009).

[49] J. Liu, H. Yuan, X.-M. Lu, and X. Wang, Quantum Fisher information matrix and multiparameter estimation, *J. Phys. A: Math. Theor.* **53**, 023001 (2019).

[50] Note that  $V_0 |\Psi_S(0)\rangle$  is unnormalized.

[51] R. Somma, G. Ortiz, J. E. Gubernatis, E. Knill, and R. Laflamme, Simulating physical phenomena by quantum networks, *Phys. Rev. A* **65**, 042323 (2002).

[52] J. Kusyk, S. M. Saeed, and M. U. Uyar, Survey on quantum circuit compilation for noisy intermediate-scale quantum computers: artificial intelligence to heuristics, *IEEE Trans. Quantum Eng.* **2**, 1 (2021).

[53] R. Kubo, Statistical-mechanical theory of irreversible processes. I. General theory and simple applications to magnetic and conduction problems, *J. Phys. Soc. Jpn.* **12**, 570 (1957).

[54] R. Zwanzig, Time-correlation functions and transport coefficients in statistical mechanics, *Annu. Rev. Phys. Chem.* **16**, 67 (1965).

[55] P. Jordan and E. Wigner, Über das paulische äquivalenzverbot, *Zeitschrift Für Physik* **47**, 631 (1928).

[56] J. Casanova, A. Mezzacapo, L. Lamata, and E. Solano, Quantum simulation of interacting fermion lattice models in trapped ions, *Phys. Rev. Lett.* **108**, 190502 (2012).

[57] J. S. Pedernales, R. Di Candia, I. L. Egusquiza, J. Casanova, and E. Solano, Efficient quantum algorithm for computing n-time correlation functions, *Phys. Rev. Lett.* **113**, 020505 (2014).

[58] F. Vatan and C. Williams, Optimal quantum circuits for general two-qubit gates, *Phys. Rev. A* **69**, 032315 (2004).

[59] Y. He, M.-X. Luo, E. Zhang, H.-K. Wang, and X.-F. Wang, Decompositions of n-qubit Toffoli gates with linear circuit complexity, *Int. J. Theor. Phys.* **56**, 2350 (2017).

[60] B. Gardas and S. Deffner, Quantum fluctuation theorem for error diagnostics in quantum annealers, *Sci. Rep.* **8**, 17191 (2018).

[61] A. Solfanelli, A. Santini, and M. Campisi, Experimental verification of fluctuation relations with a quantum computer, *PRX Quantum* **2**, 030353 (2021).

[62] K. Zhang, X. Wang, Q. Zeng, and J. Wang, Conditional entropy production and quantum fluctuation theorem of dissipative information: theory and experiments, *PRX Quantum* **3**, 030315 (2022).

[63] B. M. Escher, R. L. de Matos Filho, and L. Davidovich, General framework for estimating the ultimate precision limit in noisy quantum-enhanced metrology, *Nat. Phys.* **7**, 406 (2011).

# Supplemental Material of “Quantum Computer-Based Verification of Quantum Thermodynamic Uncertainty Relation”

## CONTENTS

List of Figures	2
I. The general TUR in Eq. (1)	2
A. Derivation	2
B. Simplification of $\mathcal{C}_F$ for specific observables	4
C. Inherent-dynamics contribution $\mathcal{C}_F$ in the weak coupling regime	5
D. Measurement of the survival activity $\mathcal{A}$	5
E. Measurement of the inherent-dynamics contribution $\mathcal{C}_F$	6
II. IBM’s quantum processors	7
III. Demonstrations on the quantum time correlator $R(T)$	8
A. Target system $S$ and CPTP map $\Phi$	8
B. Details of the circuit for measuring $R(T)$ illustrated in Fig. 1b	8
C. Application of the general TUR in Eq. (1)	9
D. Derivation of the trade-off relation on quantum time correlators in Eq. (2)	9
E. Circuits for $\mathcal{A}_G$ and $\mathcal{C}_{F_{corr}}$	10
F. Circuit transpilation and depth evaluation	11
G. Empirical results	12
IV. Demonstrations on the equality condition of the general TUR	13
A. Measurement of the optimal observable $\mathcal{F}_{opt}$	13
B. Circuits for $\mathcal{C}_{\mathcal{F}_{opt}}$	14
C. Depth evaluation	14
D. Empirical results	15
E. Comparison to the straightforward implementation for $\mathcal{C}_F$	16
F. Comparison to the Eagle processor	16
References	17

## LIST OF FIGURES

S1	Illustration of the Hadamard test . . . . .	6
S2	Naive implementation of the Hadamard tests for $\mathcal{C}_F$ . . . . .	7
S3	Circuits for state preparation and a CPTP map . . . . .	8
S4	Protocol for measuring quantum time correlators . . . . .	9
S5	Optimized circuit for measuring $\mathcal{C}_{\mathcal{F}_{\text{corr}}}$ . . . . .	11
S6	Depths of the transpiled circuits for $\mathcal{C}_{\mathcal{F}_{\text{corr}}}$ . . . . .	11
S7	Theoretical, approximated, and empirical values regarding $\mathcal{F}_{\text{corr}}$ . . . . .	12
S8	Theoretical, approximated, and empirical values of $\mathcal{A}_G$ . . . . .	12
S9	Theoretical, approximated, and empirical values of $\mathcal{C}_{\mathcal{F}_{\text{corr}}}$ . . . . .	12
S10	Circuits for $\mathcal{F}_{\text{opt}}$ , $U_{SE}$ , and $\mathcal{C}_{\mathcal{F}_{\text{opt}}}$ . . . . .	13
S11	Depths of transpiled circuits for $\mathcal{C}_{\mathcal{F}_{\text{opt}}}$ . . . . .	14
S12	Theoretical, approximated, and empirical values regarding $\mathcal{F}_{\text{opt}}$ . . . . .	15
S13	Theoretical, approximated, and empirical values of $\mathcal{A}$ . . . . .	15
S14	Theoretical, approximated, and empirical values of $\mathcal{C}_{\mathcal{F}_{\text{opt}}}$ . . . . .	15
S15	Results for $\mathcal{F}_{\text{opt}}$ with the straightforward implementation . . . . .	16
S16	Results for $\mathcal{F}_{\text{opt}}$ on the Eagle processor . . . . .	17

## I. THE GENERAL TUR IN EQ. (1)

## A. Derivation

In this section, we provide the derivation of the general TUR in Eq. (1). Generally, we assume that the initial state of the principal system  $S$  denoted by  $\rho_S(0)$  is a mixed state. The case of pure states is a special case in this general setting. Let us consider the composite system  $R + S + E$ , where  $R$  is a virtual ancillary system used to purify the initial state of the principal system  $S$ . The initial state of the composite system  $R + S + E$  is given by  $|\Psi_{RSE}(0)\rangle = |\Psi_{RS}(0)\rangle \otimes |0_E\rangle$ , where  $|\Psi_{RS}(0)\rangle = \sum_i \sqrt{p_i} |\psi_i\rangle \otimes |\psi_i\rangle$ . The reduced state on  $S$  satisfies  $\rho_S(0) = \text{Tr}_R[|\Psi_{RS}(0)\rangle \langle \Psi_{RS}(0)|]$ . The final state of the composite system  $R + S + E$  is given by  $|\Psi_{RSE}(T)\rangle = (I_R \otimes U)(|\Psi_{RS}(0)\rangle \otimes |0_E\rangle) = \sum_{im} \sqrt{p_i} |\psi_i\rangle \otimes V_m |\psi_i\rangle \otimes |\phi_m\rangle$  with Kraus operators  $\{V_m\}$  of the CPTP map  $\Phi$  for the principal system  $S$ .

To obtain the bound on the variance of the observable  $\mathcal{F}$  on  $R + S + E$ , we shall use the quantum Cramér–Rao inequality with respect to a virtual perturbation parameter  $\theta$  on the CPTP map.  $\theta$  is introduced by the following Kraus operators on  $S$  [1]:

$$V_m(\theta) = e^{\theta/2} V_m \quad (m \geq 1), \quad (\text{S1})$$

$$V_0(\theta) = U_0 \sqrt{I - e^\theta \sum_{m \geq 1}^M V_m^\dagger V_m}, \quad (\text{S2})$$

where  $U_0$  is a unitary operator appearing in the polar decomposition  $V_0 = U_0 \sqrt{V_0^\dagger V_0}$ . The original Kraus operators  $\{V_m\}$  are recovered when  $\theta = 0$ . With the quantum Fisher information (QFI)  $J(\theta)$ , the quantum Cramér–Rao inequality is given as follows [2, 3]:

$$\frac{\text{Var}[\mathcal{F}]_\theta}{(\partial_\theta \langle \mathcal{F} \rangle_\theta)^2} \geq \frac{1}{J(\theta)}, \quad (\text{S3})$$

where the QFI is

$$J(\theta) = 4 \left[ \langle \Psi_{RSE}(0) | H_1(\theta) | \Psi_{RSE}(0) \rangle - \langle \Psi_{RSE}(0) | H_2(\theta) | \Psi_{RSE}(0) \rangle^2 \right], \quad (\text{S4})$$

with

$$H_1(\theta) = I_R \otimes \sum_{m=0}^M \frac{dV_m^\dagger(\theta)}{d\theta} \frac{dV_m}{d\theta} \otimes I_E, \quad (\text{S5})$$

$$H_2(\theta) = I_R \otimes i \sum_{m=0}^M \frac{dV_m^\dagger(\theta)}{d\theta} V_m(\theta) \otimes I_E. \quad (\text{S6})$$

Note that the  $i$  in the second equality represents the imaginary unit and should be distinguished from  $i$  used as an index.

The QFI  $J(\theta = 0)$  is calculated as [1]

$$\begin{aligned} J(\theta = 0) &= \text{Tr}[\rho_S(0)(V_0^\dagger V_0)^{-1}] - 1 \\ &= \mathcal{A}. \end{aligned} \quad (\text{S7})$$

Next, we calculate the scaling,  $\partial_\theta \langle \mathcal{F} \rangle_\theta$ , of the expectation value of the observable  $\mathcal{F}$  with respect to the virtual perturbation parameter  $\theta$ .  $\langle \mathcal{F} \rangle_\theta$  is given by

$$\begin{aligned} \langle \mathcal{F} \rangle_\theta &= \langle \Psi_{RSE}(T) | \mathcal{F} | \Psi_{RSE}(T) \rangle \\ &= \left( \sum_{ik} \sqrt{p_i} \langle \psi_i | \otimes \langle \psi_i | V_k(\theta)^\dagger \otimes \langle \phi_k | \right) \mathcal{F} \left( \sum_{jl} \sqrt{p_j} | \psi_j \rangle \otimes V_l(\theta) | \psi_j \rangle \otimes | \phi_l \rangle \right). \end{aligned} \quad (\text{S8})$$

The derivative of  $\langle \mathcal{F} \rangle_\theta$  with respect to  $\theta$  is given by

$$\begin{aligned} \partial_\theta \langle \mathcal{F} \rangle_\theta &= \left( \sum_{ik} \sqrt{p_i} \langle \psi_i | \otimes \langle \psi_i | \frac{dV_k(\theta)^\dagger}{d\theta} \otimes \langle \phi_k | \right) \mathcal{F} \left( \sum_{jl} \sqrt{p_j} | \psi_j \rangle \otimes V_l(\theta) | \psi_j \rangle \otimes | \phi_l \rangle \right) \\ &\quad + \left( \sum_{ik} \sqrt{p_i} \langle \psi_i | \otimes \langle \psi_i | V_k(\theta)^\dagger \otimes \langle \phi_k | \right) \mathcal{F} \left( \sum_{jl} \sqrt{p_j} | \psi_j \rangle \otimes \frac{dV_l(\theta)}{d\theta} | \psi_j \rangle \otimes | \phi_l \rangle \right) \\ &= \left( \sum_{ik} \sqrt{p_i} \langle \psi_i | \otimes \langle \psi_i | \frac{dV_k(\theta)^\dagger}{d\theta} \otimes \langle \phi_k | \right) \mathcal{F} \left( \sum_{jl} \sqrt{p_j} | \psi_j \rangle \otimes V_l(\theta) | \psi_j \rangle \otimes | \phi_l \rangle \right) + \text{h.c.} \end{aligned} \quad (\text{S9})$$

For  $k > 0$ , the derivative of  $V_k(\theta)$  is given by

$$\frac{dV_k(\theta)}{d\theta} = \frac{1}{2} e^{\theta/2} V_k(\theta) = \bigg|_{\theta=0} = \frac{1}{2} V_k. \quad (\text{S10})$$

For  $k = 0$ , we need some calculations to obtain the derivative. First, we introduce the spectral decomposition of  $\sum_{m>0}^M V_m^\dagger V_m$  as

$$\sum_{m>0}^M V_m^\dagger V_m = \sum_n \zeta_n \Pi_n, \quad (\text{S11})$$

where  $\zeta_n$  is the eigenvalue of  $\sum_{m>0}^M V_m^\dagger V_m$  and  $\Pi_n$  is the projection operator onto the eigenspace of  $\zeta_n$ . Then, we can write  $V_0(\theta)$  as

$$V_0(\theta) = U_0 \sum_n \sqrt{1 - e^\theta \zeta_n} \Pi_n. \quad (\text{S12})$$

Using this equation, we can calculate the derivative of  $\frac{dV_0(\theta)}{d\theta}$  as

$$\begin{aligned} \frac{dV_0(\theta)}{d\theta} &= \frac{1}{2} U_0 \sum_n \frac{-\zeta_n e^{\theta/2}}{\sqrt{1 - e^\theta \zeta_n}} \Pi_n \\ &= \bigg|_{\theta=0} \frac{1}{2} U_0 \sum_n \frac{-\zeta_n}{\sqrt{1 - \zeta_n}} \Pi_n \\ &= \frac{1}{2} U_0 \sum_n \sqrt{1 - \zeta_n} \Pi_n - \frac{1}{2} U_0 \sum_n \frac{1}{\sqrt{1 - \zeta_n}} \Pi_n \\ &= \frac{1}{2} V_0 - \frac{1}{2} V_0^{\dagger -1}. \end{aligned} \quad (\text{S13})$$

Thus we obtain the derivative of  $\langle \mathcal{F} \rangle_\theta$  as

$$\begin{aligned}
\partial_\theta \langle \mathcal{F} \rangle_{\theta=0} &= \frac{1}{2} \left( \sum_{ik} \sqrt{p_i} \langle \psi_i | \otimes \langle \psi_i | V_k^\dagger \otimes \langle \phi_k | \right) \mathcal{F} \left( \sum_{jl} \sqrt{p_j} | \psi_j \rangle \otimes V_l | \psi_j \rangle \otimes | \phi_l \rangle \right) \\
&\quad - \frac{1}{2} \left( \sum_i \sqrt{p_i} \langle \psi_i | \otimes \langle \psi_i | V_0^{-1} \otimes \langle \phi_0 | \right) \mathcal{F} \left( \sum_{jl} \sqrt{p_j} | \psi_j \rangle \otimes V_l | \psi_j \rangle \otimes | \phi_l \rangle \right) \\
&\quad + (\text{h.c. of the first and second terms}) \\
&= \left( \sum_{ik} \sqrt{p_i} \langle \psi_i | \otimes \langle \psi_i | V_k^\dagger \otimes \langle \phi_k | \right) \mathcal{F} \left( \sum_{jl} \sqrt{p_j} | \psi_j \rangle \otimes V_l | \psi_j \rangle \otimes | \phi_l \rangle \right) \\
&\quad - \frac{1}{2} \left( \sum_i \sqrt{p_i} \langle \psi_i | \otimes \langle \psi_i | V_0^{-1} \otimes \langle \phi_0 | \right) \mathcal{F} \left( \sum_{jl} \sqrt{p_j} | \psi_j \rangle \otimes V_l | \psi_j \rangle \otimes | \phi_l \rangle \right) \\
&\quad - \frac{1}{2} \left( \sum_{ik} \sqrt{p_i} \langle \psi_i | \otimes \langle \psi_i | V_k^\dagger \otimes \langle \phi_k | \right) \mathcal{F} \left( \sum_j \sqrt{p_j} | \psi_j \rangle \otimes V_0^{\dagger^{-1}} | \psi_j \rangle \otimes | \phi_0 \rangle \right) \\
&= \langle \mathcal{F} \rangle - \frac{1}{2} \langle \tilde{\Psi}_{RSE}(0) | \mathcal{F} | \Psi_{RSE}(T) \rangle - \frac{1}{2} \langle \Psi_{RSE}(T) | \mathcal{F} | \tilde{\Psi}_{RSE}(0) \rangle \\
&= \langle \mathcal{F} \rangle - \mathcal{C}_{\mathcal{F}}, \tag{S14}
\end{aligned}$$

where  $|\tilde{\Psi}_{RSE}(0)\rangle = (I_R \otimes V_0^{\dagger^{-1}} \otimes I_E) |\Psi_{RS}(0)\rangle \otimes |\phi_0\rangle$  and  $\mathcal{C}_{\mathcal{F}} = \text{Re}[\langle \tilde{\Psi}_{RSE}(0) | \mathcal{F} | \Psi_{RSE}(T) \rangle]$ . Combining Eqs. (S3), (S7), and (S14), we obtain the general TUR in Eq. (1) for  $R+S+E$ . To obtain the bound for  $S+E$  as in the main text, we trace out the auxiliary system  $R$ . In the following, we denote  $\mathcal{C}_{\mathcal{F}}$  as  $\mathcal{C}_{\mathcal{F}} = \text{Re}[\langle \tilde{\Psi}_{SE}(0) | \mathcal{F} | \Psi_{SE}(T) \rangle]$  for brevity, but it can be readily generalized to the case of a mixed state on  $S+E$ .

Several points should be noted regarding the above derivation. First, it holds for a generic observable  $\mathcal{F}$  on the composite system  $R + S + E$ . In practice, we can choose  $\mathcal{F}$  to be an observable solely on the system  $S + E$ , as the ancillary system  $R$  is virtual. Second, when the initial state of  $S$  is pure, we substitute  $|\Psi_{RS}(0)\rangle = |\Psi_S(0)\rangle \otimes |\Psi_S(0)\rangle$  into the derivation. Third, the equality condition of the general TUR comes from that of the quantum Cramér–Rao inequality in Eq. (S3). The equality in Eq. (S3) is attained when the observable  $\mathcal{F}$  is proportional to the symmetric logarithmic derivative  $\mathcal{L}$  with respect to the Kraus operators and the perturbation parameter  $\theta$  [2]. Consequently, the equality condition of the general TUR is satisfied when  $\mathcal{F}$  commutes with  $\mathcal{L}$ . This condition can be fulfilled by considering observables solely on  $S + E$  when the initial state of  $S$  is pure.

## B. Simplification of $\mathcal{C}_{\mathcal{F}}$ for specific observables

For a separable observable  $\mathcal{F}^{\text{sep}}$  on the composite system  $S + E$ , the inherent-dynamics contribution  $\mathcal{C}_{\mathcal{F}}$  in the general TUR (Eq. (1)) takes a simplified form.  $\mathcal{F}^{\text{sep}}$  can be written as  $\mathcal{F}^{\text{sep}} = \sum_{l,m} f_{lm} |\phi_l^{(S)}\rangle\langle\phi_l^{(S)}| \otimes |\phi_m^{(E)}\rangle\langle\phi_m^{(E)}|$ , with  $|\phi_l^{(S)}\rangle$  and  $|\phi_m^{(E)}\rangle$  being the eigenbases of subsystems  $S$  and  $E$ . We define the Kraus operators  $\{V_m\}$  by the basis  $|\phi_m^{(E)}\rangle$ . In this case,  $\mathcal{C}_{\mathcal{F}}$  reduces to

$$\begin{aligned}
\mathcal{C}_{\mathcal{F}^{\text{sep}}} &= \text{Re}[\langle \Psi_{SE}(0) | (I_R \otimes V_0^{-1} \otimes I_E) \mathcal{F}^{\text{sep}} | \Psi_{SE}(T) \rangle] \\
&= \text{Re}[\text{Tr}[\rho_S(0)(V_0^{-1} \mathcal{F}_0^{\text{sep}} V_0)]], \tag{S15}
\end{aligned}$$

where  $\mathcal{F}_0^{\text{sep}} = \sum_k f_{k0} |\phi_k^{(S)}\rangle\langle\phi_k^{(S)}|$  is the observable  $\mathcal{F}^{\text{sep}}$  conditioned on the environment  $E$  being in the state  $|\phi_0^{(E)}\rangle$ . For local observables  $\mathcal{F}_S$  acting solely on subsystem  $S$ , a further simplification yields

$$\mathcal{C}_{\mathcal{F}_S} = \text{Re}[\text{Tr}[\rho_S(0)(V_0^{-1} \mathcal{F}_S V_0)]]. \tag{S16}$$

Notably, this expression for  $\mathcal{C}_{\mathcal{F}_S}$  only involves the Kraus operator  $V_0$  from the set  $\{V_m\}$  that defines the unitary evolution  $U_{SE}$  of the composite system. We will utilize the expression of  $\mathcal{C}_{\mathcal{F}_S}$  for the demonstrations on quantum time correlators.

For local observables  $\mathcal{F}_E = \sum_m f_m |\phi_m^{(E)}\rangle\langle\phi_m^{(E)}|$  on  $E$ ,  $\mathcal{C}_{\mathcal{F}_E}$  becomes a constant as  $\mathcal{C}_{\mathcal{F}_E} = f_0$ . In particular, when  $\mathcal{F}_E$  is a counting observable, which satisfies  $f_0 = 0$ ,  $\mathcal{C}_{\mathcal{F}_E}$  vanishes and the general TUR reduces to the previous TUR [1].

### C. Inherent-dynamics contribution $\mathcal{C}_{\mathcal{F}}$ in the weak coupling regime

In this section, we consider the weak coupling regime between a principal system  $S$  and an environment  $E$ , where the dynamics on  $S$  is nearly unitary. In this case, the Kraus operator  $V_0$  is almost unitary and satisfies  $V_0^\dagger V_0 = I - \epsilon$ , where  $\epsilon$  is an operator with a small norm. Using polar decomposition,  $V_0$  can be expressed in terms of  $\epsilon$  as  $V_0 = U_0 \sqrt{V_0^\dagger V_0} = U_0 \sqrt{I - \epsilon}$ , where  $U_0$  is a unitary operator. We can approximate  $V_0$  as  $V_0 \approx U_0(I - \frac{1}{2}\epsilon)$ , and its inverse as  $V_0^{-1} \approx (I + \frac{1}{2}\epsilon)U_0^\dagger$ . Using this approximation,  $\mathcal{C}_{\mathcal{F}}$  can be approximated as

$$\begin{aligned}\mathcal{C}_{\mathcal{F}} &\approx \text{Re}[\langle\Psi_S(0)| (I + \frac{1}{2}\epsilon)U_0^\dagger \otimes \langle\phi_0| \mathcal{F}U_{SE} |\Psi_{SE}(0)\rangle] \\ &= \text{Re}[\langle\Psi_S(0)| U_0^\dagger \otimes \langle\phi_0| \mathcal{F}U_{SE} |\Psi_{SE}(0)\rangle] + \frac{1}{2}\text{Re}[\langle\Psi_S(0)| \epsilon U_0^\dagger \otimes \langle\phi_0| \mathcal{F}U_{SE} |\Psi_{SE}(0)\rangle]\end{aligned}\quad (\text{S17})$$

For local observables on  $S$ , where  $\mathcal{C}_{\mathcal{F}}$  simplifies to Eq. (S16), we obtain

$$\begin{aligned}\mathcal{C}_{\mathcal{F}_S} &\approx \text{Re}[\langle\Psi_S(0)| (I - \frac{1}{2}\epsilon + \epsilon)U_0^\dagger \mathcal{F}_S V_0 |\Psi_S(0)\rangle] \\ &= \langle\Psi_S(0)| V_0^\dagger \mathcal{F}_S V_0 |\Psi_S(0)\rangle + \text{Re}[\langle\Psi_S(0)| \epsilon U_0^\dagger \mathcal{F}_S V_0 |\Psi_S(0)\rangle] \\ &\approx \langle\Psi_S(0)| V_0^\dagger \mathcal{F}_S V_0 |\Psi_S(0)\rangle + \text{Re}[\langle\Psi_S(0)| \epsilon U_0^\dagger \mathcal{F}_S U_0 |\Psi_S(0)\rangle].\end{aligned}\quad (\text{S18})$$

Thus, the primary term of  $\mathcal{C}_{\mathcal{F}_S}$  is the expectation value of  $\mathcal{F}_S$  under the non-trace-preserving dynamics described by  $V_0$ .

### D. Measurement of the survival activity $\mathcal{A}$

In this section, we present a methodology to quantify the survival activity  $\mathcal{A}$ , defined as  $\mathcal{A} = \text{Tr}[\rho_S(0)(V_0^\dagger V_0)^{-1}] - 1$  in the general TUR given by Eq. (1). We begin by assuming the feasibility of applying the inverse unitary operation,  $U_{SE}^\dagger$ , on the combined system and environment  $S+E$ , and that both the initial and final states on  $E$  defining  $V_0$  are given by  $|0\rangle$ . Later, we discuss the scenario where the reversibility of the unitary transformation associated with the CPTP map on  $S$  is not available.

Using the completeness condition of the Kraus operators  $\{V_m\}$ , we define an operator  $\epsilon = \sum_{m \geq 0} V_m^\dagger V_m = I - V_0^\dagger V_0$ . The Neumann series expansion of  $(V_0^\dagger V_0)^{-1}$  is given by

$$(V_0^\dagger V_0)^{-1} = (I - \epsilon)^{-1} = \sum_{n=0}^{\infty} \epsilon^n = \sum_{n=0}^{\infty} (I - V_0^\dagger V_0)^n. \quad (\text{S19})$$

Applying the binomial expansion, we obtain

$$(V_0^\dagger V_0)^{-1} = \sum_{n=1}^{\infty} \sum_{k=0}^n (-1)^k \binom{n}{k} (V_0^\dagger V_0)^k + 1. \quad (\text{S20})$$

Using this expansion, the survival activity  $\mathcal{A}$  can be expressed as

$$\begin{aligned}\mathcal{A} &= \sum_{n=1}^{\infty} \sum_{k=0}^n (-1)^k \binom{n}{k} \text{Tr}[\rho_S(0)(V_0^\dagger V_0)^k] \\ &= \lim_{N \rightarrow \infty} \sum_{n=0}^N (-1)^n \binom{N+1}{n+1} \text{Tr}[\rho_S(0)(V_0^\dagger V_0)^n] - 1\end{aligned}\quad (\text{S21})$$

Thus, the survival activity is determined by evaluating the expectation values  $\text{Tr}[\rho_S(0)(V_0^\dagger V_0)^n]$ . An approximate value for the survival activity can be obtained by truncating the series at a finite  $N$ , yielding an  $O(N)$  approximation

in terms of the norm of  $\epsilon$ , which represents the interaction strength between the system  $S$  and the environment  $E$ . We note that truncating at  $N$  in Eq. (S21) is justified because it is equivalent to truncating at  $n = N$  in Eq. (S19), which clarifies the order of  $\epsilon$ .

Consider truncating the summation over  $n$  at  $N$ . We present a protocol to measure  $\text{Tr}[\rho_S(0)(V_0^\dagger V_0)^N]$ , which allows for the simultaneous measurement of  $\text{Tr}[\rho_S(0)(V_0^\dagger V_0)^n]$  for all  $n < N$ . We define an unnormalized state  $\rho_S^{(n)}$  that satisfies  $\text{Tr}[\rho_S^{(n)}] = \text{Tr}[\rho_S(0)(V_0^\dagger V_0)^n]$ . The initial state  $\rho_S^{(0)}$  is given by  $\rho_S^{(0)} = \rho_S(0)$ . For  $n > 0$ , the state  $\rho_S^{(n)}$  is iteratively constructed as

$$\rho_S^{(n+1)} = \begin{cases} V_0 \rho_S^{(n)} V_0^\dagger & \text{if } n \text{ is even,} \\ V_0^\dagger \rho_S^{(n)} V_0 & \text{if } n \text{ is odd.} \end{cases} \quad (\text{S22})$$

Here, we exploit the cyclic property of the trace to obtain these relationships. For even  $n$ ,  $\rho_S^{(n+1)}$  is obtained by evolving  $\rho_S^{(n)}$  under the operator  $V_0$ : first apply  $U_{SE}$  to  $\rho_S^{(n)} \otimes |0\rangle\langle 0|$ , and then project onto the environmental state  $|0\rangle$ . For odd  $n$ , a similar process is employed using  $V_0^\dagger$ . The evolution with  $V_0^\dagger$  follows from the definition of  $V_0$ , given by  $V_0 = (I_S \otimes |0\rangle\langle 0|)U_{SE}(I_S \otimes |0\rangle\langle 0|)$ . Consequently,  $V_0^\dagger$  is defined as  $V_0^\dagger = (I_S \otimes |0\rangle\langle 0|)U_{SE}^\dagger(I_S \otimes |0\rangle\langle 0|)$ , which can be realized by first applying  $U_{SE}^\dagger$  to  $\rho_S^{(n)} \otimes |0\rangle\langle 0|$ , followed by a projection onto the environmental state  $|0\rangle$ .

To evaluate  $\text{Tr}[\rho_S(0)(V_0^\dagger V_0)^N]$ , we initialize the principal system  $S$  in the state  $\rho_S(0)$  and prepare  $N$  replicas of the environmental system  $E$  in the state  $|0\rangle$ . We then apply either  $U_{SE}$  or  $U_{SE}^\dagger$  to  $S$  and each environmental replica  $E^{(n)}$  according to the sequence prescribed by Eq. (S22). After performing this sequence of operations  $N$  times, we measure the environmental systems in the basis  $\{|0\rangle, |1\rangle\}$  and record the instances where all environments are found in the state  $|0\rangle$ . By repeating this procedure multiple times, we obtain an estimate of the probability of such occurrences, from which we can infer the desired expectation value  $\text{Tr}[\rho_S(N)(V_0^\dagger V_0)^N]$ . Importantly, this approach allows us to simultaneously obtain the expectations  $\text{Tr}[\rho_S(0)(V_0^\dagger V_0)^n]$  for all  $n < N$  using the same outcomes, simply by considering only the first  $n$  environmental systems in each instance. Finally, the survival probability can be calculated using Eq. (S21) based on these expectation values.

We provide two additional insights regarding the protocol. First, the protocol could be implemented using only a single environmental system by incorporating measurements within each iteration. After applying  $U_{SE}$  or  $U_{SE}^\dagger$ , we measure the environment in the  $\{|0\rangle, |1\rangle\}$  basis. If the outcome is  $|0\rangle$ , we proceed to the next iteration; if the outcome is  $|1\rangle$ , we discard the result and restart the protocol from the beginning. By keeping track of the number of successful iterations, we can estimate the expectation values  $\text{Tr}[\rho_S(0)(V_0^\dagger V_0)^n]$  for all  $n \leq N$ . Second, the survival activity  $\mathcal{A}$  can be approximated without applying  $U_{SE}^\dagger$ . By truncating the expansion in Eq. (S21) at  $N = 1$ , we obtain the approximation  $\mathcal{A} \approx 1 - \text{Tr}[\rho_S(0)V_0^\dagger V_0]$ . This approximation is valid in the regime where the interaction between systems  $S$  and  $E$  is weak, as higher-order terms in the expansion become negligible in this case.

### E. Measurement of the inherent-dynamics contribution $\mathcal{C}_F$

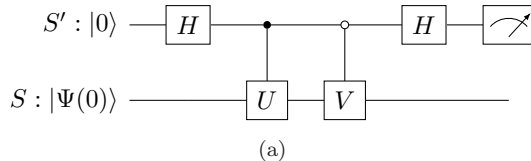


FIG. S1. Illustration of the Hadamard test for measuring  $\text{Re}[\langle \Psi(0) | V^\dagger U | \Psi(0) \rangle]$ .

The inherent-dynamics contribution  $\mathcal{C}_F$  can be measured using an approximation method similar to that used for the survival activity  $\mathcal{A}$ . Recall the definition of  $\mathcal{C}_F$ :  $\mathcal{C}_F = \text{Re}[\langle \tilde{\Psi}_{SE}(0) | \mathcal{F} | \Psi_{SE}(T) \rangle]$  with the unnormalized state  $|\tilde{\Psi}_{SE}(0)\rangle = (V_0^{-1})^\dagger |\Psi_S(0)\rangle \otimes |\phi_0\rangle$ . We rewrite  $\mathcal{C}_F$  as

$$\mathcal{C}_F = \text{Re}[\langle \Psi_S(0) | \otimes \langle \phi_0 | (V_0^{-1} \otimes I_E) \mathcal{F} U_{SE} |\Psi_S(0)\rangle \otimes |0_E\rangle]. \quad (\text{S23})$$

We further calculate it to obtain the expression  $(V_0 V_0^\dagger)^{-1}$  as

$$\mathcal{C}_F = \text{Re}[\langle \Psi_S(0) | V_0^\dagger \otimes \langle \phi_0 | ((V_0 V_0^\dagger)^{-1} \otimes I_E) \mathcal{F} U_{SE} |\Psi_S(0)\rangle \otimes |0_E\rangle]. \quad (\text{S24})$$

By the Neumann series expansion as in the previous section for  $\mathcal{A}$ , we can approximate  $(V_0 V_0^\dagger)^{-1}$  as  $(V_0 V_0^\dagger)^{-1} \approx 2I - V_0 V_0^\dagger$  by truncating at  $N = 1$  in Eq. (S19). Subsequently, we obtain the following first-order approximation:

$$\mathcal{C}_F \approx 2C_1 - C_2, \quad (\text{S25})$$

where

$$C_1 = \text{Re}[\langle \Psi_S(0) | V_0^\dagger \otimes \langle \phi_0 | \mathcal{F} U_{SE} | \Psi_S(0) \rangle \otimes | 0_E \rangle], \quad (\text{S26})$$

$$C_2 = \text{Re}[\langle \Psi_S(0) | V_0^\dagger \otimes \langle \phi_0 | (V_0 V_0^\dagger \otimes I_E) \mathcal{F} U_{SE} | \Psi_S(0) \rangle \otimes | 0_E \rangle]. \quad (\text{S27})$$

To measure the correlators  $C_1$  and  $C_2$ , we employ the Hadamard test [4]. Let us illustrate the test with a simple example of measuring  $\text{Re}[\langle \Psi(0) | V^\dagger U | \Psi(0) \rangle]$ , as shown in Fig. S1. In this test, we introduce an ancilla qubit  $S'$  prepared in the state  $|+\rangle$ . The ancilla is then entangled with the system  $S$  using a controlled- $U$  operation, which applies the unitary operator  $U$  to the system only when the control qubit  $S'$  is in the state  $|1\rangle$ . Next, a controlled- $V$  operation is applied, where the control is denoted by a white circle in the figure. This operation applies the unitary operator  $V$  to the system  $S$  only when the ancilla qubit  $S'$  is in the state  $|0\rangle$ . Finally, to obtain  $\text{Re}[\langle \Psi(0) | V^\dagger U | \Psi(0) \rangle]$ , we measure the expectation value of the Pauli operator  $\sigma_x$  on the ancilla qubit  $S'$ . In practice, this measurement can be realized by applying an Hadamard gate followed by a  $\sigma_z$  measurement on  $S'$ . The Hadamard test provides a systematic approach to measure correlators by applying controlled unitary operations. By extending this method, we can measure the correlators  $C_1$  and  $C_2$  in our study.

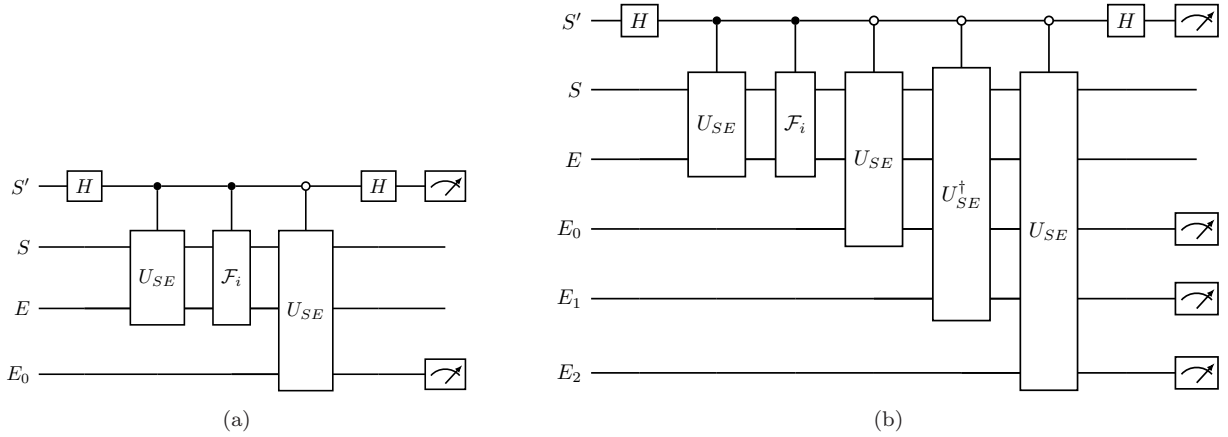


FIG. S2. Naive implementation of the circuits for the Hadamard tests to measure  $\mathcal{C}_F$ . (a) Circuit for  $C_1$ . (b) Circuit for  $C_2$ . All measurements are made in the computational basis  $\{|0\rangle, |1\rangle\}$ . The white control represents applying the target unitary operator when the control qubit is in the state  $|0\rangle$ .

The straightforward implementations of the Hadamard tests for  $C_1$  and  $C_2$  is illustrated in Figs. S2a and S2b, respectively. To apply  $V_0$  to the system  $S$ , we first apply  $U_{SE}$  with the environment  $E$  initialized in the state  $|0\rangle$  and then postselect the cases where the measurement outcome of  $E$  is  $|0\rangle$ . To measure  $C_1$ , we sequentially apply controlled versions of  $U_{SE}$ ,  $\mathcal{F}_i$  (a unitary operation satisfying  $\sum_i \mathcal{F}_i = \mathcal{F}$ ), and another  $U_{SE}$  with a new environment. Similarly,  $C_2$  can be measured using additional controlled  $U_{SE}$  operations and environments.

However, the straightforward implementations of the Hadamard tests for  $C_1$  and  $C_2$  are impractical for real processors due to their excessive depths. Controlled unitary operations involving three or more qubits are generally challenging to implement when only single or two-qubit gates on sparsely connected qubits are available on real hardware. To address the issue of circuit depth, we develop shallow circuits to measure  $C_1$  and  $C_2$  by leveraging the structure of the observable  $\mathcal{F}$  and the operator  $V_0$ . These circuits are detailed in the sections III E for the  $R(T)$  demonstration and IV B for the demonstration on the equality condition of the general TUR. We quantitatively evaluate the circuit depths in the sections III F for the former demonstration and IV C for the latter demonstration.

## II. IBM'S QUANTUM PROCESSORS

We test the general TUR in Eq. (1) and the thermodynamic bound on the time correlator  $R(T)$  in Eq. (2) using a superconducting qubit system from IBM's "Heron" quantum processor (ibm\_torino) [5, 6]. The processor comprises

133 transmon qubits [7], each connected to two or three neighboring qubits, and all initialized in the state  $|0\rangle$ . The system supports five native gates: Identity, X, SX (the square root of X), RZ, and the two-qubit CZ (controlled Z) gate. Other gates are built from these primitive gates. Although we describe operations using non-native gates like RX and RY in the following, the circuits containing these gates are transpiled before execution on the quantum processor. Since only the measurement of  $\sigma_z$  is available for the qubits, an Hadamard gate and  $\sigma_z$  measurement are used to measure  $\sigma_x$ .

The qubits and gates on the `ibm_torino` processor were calibrated daily during our demonstrations in May 2024. Over this period, the processor's typical metrics [8] were as follows: median CZ error of  $(4.56 \pm 0.19) \times 10^{-3}$ , median SX error of  $(3.15 \pm 0.15) \times 10^{-4}$ , median readout error of  $(1.95 \pm 0.10) \times 10^{-2}$ , median T1 time of  $(167.73 \pm 6.14)\mu\text{s}$ , and median T2 time of  $(130.19 \pm 5.90)\mu\text{s}$ . These metrics exhibited no significant fluctuations throughout the course of our demonstrations.

To compare empirical results across different quantum processors, we also conducted demonstrations for the equality condition of the general TUR on IBM's previous-generation quantum processor called "Eagle" (`ibm_sherbrooke`) [5, 9]. Unlike the Heron processor, the Eagle processor employs the echo cross resonance (ECR) gate [10] as a native two-qubit gate, although it has the same qubit connectivity as the Heron processor. During the demonstration period, the typical metrics of `ibm_sherbrooke` were as follows: median ECR error of  $(7.75 \pm 0.43) \times 10^{-3}$ , median SX error of  $(2.31 \pm 0.13) \times 10^{-4}$ , median readout error of  $(1.14 \pm 0.09) \times 10^{-2}$ , median T1 time of  $(268.19 \pm 7.96)\mu\text{s}$ , and median T2 time of  $(182.58 \pm 7.35)\mu\text{s}$ . Benchmarks of the Heron and Eagle processors are provided in Ref. [11].

### III. DEMONSTRATIONS ON THE QUANTUM TIME CORRELATOR $R(T)$

#### A. Target system $S$ and CPTP map $\Phi$

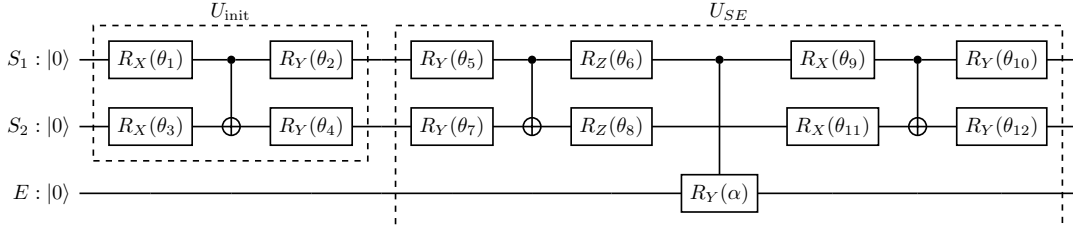


FIG. S3. Circuits for preparing the initial state  $\rho_S(0)$  and constructing the CPTP map  $\Phi$ . The initial state  $\rho_S(0)$  is generated by applying a randomly parameterized unitary gate  $U_{\text{init}}$  to the ground state  $|0\rangle \otimes |0\rangle$  of the system  $S$ . The CPTP map  $\Phi$  acting on the system  $S$  is realized by applying a unitary operator  $U_{SE}$  to the composite system  $S+E$ , where  $U_{SE}$  comprises randomly parameterized rotation gates.

In this demonstration, we consider a principal system  $S$  comprising two qubits and an environment with one qubit. Figure S3 illustrates the unitary operator  $U_{\text{init}}$  for state preparation and  $U_{SE}$  for a CPTP map  $\Phi$  on  $S$ . The operator  $U_{\text{init}}$  comprises two rotations around the X-axis (RX), one CNOT (controlled X) gate, and two rotations around the Y-axis (RY). Each rotation gate is parameterized by  $\theta_i$  for  $i = 1, \dots, 4$ , which is randomly selected from the interval  $[0, \pi/2]$ . Similarly,  $U_{SE}$  comprises single-qubit rotation gates randomly parameterized by  $\theta_i$  for  $i = 5, \dots, 12$ , chosen from the same interval. Additionally,  $U_{SE}$  includes a controlled RY gate with the control qubit on  $S$  and the target qubit on  $E$ . To modulate the interaction strength between  $S$  and  $E$ , we use a parameter  $\gamma$  chosen from the interval  $[0, 0.5]$ , setting the rotation by the controlled RY gate to  $\alpha = \pi\gamma/2$ . In the following demonstrations, we fix and investigate 50 sets of the parameters  $\{\theta_i\}$  and  $\gamma$ .

#### B. Details of the circuit for measuring $R(T)$ illustrated in Fig. 1b

We focus on the two-point time correlator  $R(t) = \langle \mathcal{H}(t)\mathcal{G}(0) \rangle_{\rho_S(0)}$  of unitary observables  $\mathcal{G}$  and  $\mathcal{H}$ , where  $\mathcal{H}(t) = \sum_m V_m^\dagger \mathcal{H} V_m$  is the Heisenberg picture of  $\mathcal{H}$  at time  $t$ . We apply the general TUR to a circuit for the protocol to measure  $R(t)$ , which is illustrated in Fig. 1b. This protocol, based on Ref. [12], employs the Hadamard test described above. The main part of the circuit for the protocol is shown in Fig. S4 and can be described as follows:

1. Initialize an auxiliary qubit  $S'$  in the state  $|0\rangle$ .

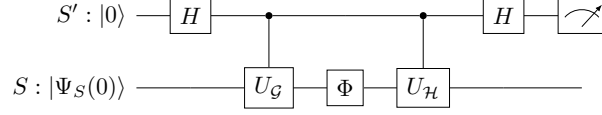


FIG. S4. Schematic representation of the protocol for measuring quantum time correlators. The ancillary system  $S'$  is a qubit, while the principal system  $S$  undergoes a CPTP map  $\Phi$ . The map is interspersed between the controlled unitary operations  $U_G^{(c)}$  and  $U_H^{(c)}$ , which are applied to the combined system  $S' + S$ .

2. Apply an Hadamard gate to  $S'$  to obtain the state  $|+\rangle = \frac{1}{\sqrt{2}}(|0\rangle + |1\rangle)$ .
3. Perform a controlled unitary operation  $U_G^{(c)}$  on the combined system  $S + S'$ , which applies  $\mathcal{G}$  on  $S$  conditioned on the state of  $S'$ .
4. Subject the main system  $S$  to the CPTP map  $\Phi$ .
5. Perform a controlled unitary operation  $U_H^{(c)}$  on  $S + S'$ , which applies  $\mathcal{H}$  on  $S$  conditioned on the state of  $S'$ .
6. Measure the ancilla  $S'$  to obtain the expectation values of the Pauli operators  $\sigma_x$  and  $\sigma_y$ , which correspond to the real and imaginary components of  $R(t)$ , respectively. Note that due to hardware constraints, the  $\sigma_x$  measurement is performed by applying an Hadamard gate followed by a  $\sigma_z$  measurement.

Let the final state of the composite system prior to measurement be denoted as  $|\Psi_{S'S}(T)\rangle$ . The time correlator  $R(t)$  satisfies

$$R(T) = \text{Tr}[\rho_S(0)\mathcal{H}(T)\mathcal{G}(0)] = \langle \Psi_{S'S}(T) | \sigma_x \otimes I_S | \Psi_{S'S}(T) \rangle + i \langle \Psi_{S'S}(T) | \sigma_y \otimes I_S | \Psi_{S'S}(T) \rangle. \quad (\text{S28})$$

Therefore, by measuring the Pauli operators  $\sigma_x$  and  $\sigma_y$  on the ancillary system  $S'$ , we can extract the real and imaginary components of  $R(T)$ , respectively. In the following, we focus on the real component  $\text{Re}[R(T)]$ .

### C. Application of the general TUR in Eq. (1)

We apply the general TUR in Eq. (1) to investigate the precision and thermodynamic cost of the protocol described above. The generality of the TUR allows us to consider arbitrary observables. As depicted in Fig. 1b, we treat the intermediate state  $\rho_{S'S}^{\mathcal{G}} = U_G^{(c)}(|+\rangle\langle+| \otimes \rho_S(0))U_G^{(c)\dagger}$  as the initial state and the observable  $\mathcal{F}_{\text{corr}} = U_H^{(c)}(\sigma_x \otimes I_S)U_H^{(c)\dagger}$  as the observable to be bounded, which satisfies  $\langle \mathcal{F}_{\text{corr}} \rangle = \text{Re}[R(T)]$ . The survival activity for the CPTP map  $\Phi$  is given by  $\mathcal{A}_{\mathcal{G}} = \text{Tr}[\rho_{S'S}^{\mathcal{G}}(V_0^\dagger V_0)^{-1}] - 1$ , and the inherent-dynamics contribution is

$$\mathcal{C}_{\mathcal{F}_{\text{corr}}} = \text{Re}[\langle \tilde{\Psi}_{SE}(0) | \mathcal{F}_{\text{corr}} | \Psi_{SE}(T) \rangle] = \text{Re}[\text{Tr}[\rho_{S'S}^{V_0}(V_0 V_0^\dagger)^{-1} \mathcal{F}_{\text{corr}}]], \quad (\text{S29})$$

where  $\rho_{S'S}^{V_0} = (I_{S'} \otimes V_0)\rho_{S'S}^{\mathcal{G}}(I_{S'} \otimes V_0^\dagger)$ . We note that the derivation of  $\mathcal{C}_{\mathcal{F}_{\text{corr}}}$  is based on  $\mathcal{C}_{\mathcal{F}}$  for  $\mathcal{F}_S$  in Eq. (S16). For these quantities, the general TUR holds as

$$\frac{\text{Var}[\mathcal{F}_{\text{corr}}]}{(\langle \mathcal{F}_{\text{corr}} \rangle - \mathcal{C}_{\mathcal{F}_{\text{corr}}})^2} \geq \frac{1}{\mathcal{A}_{\mathcal{G}}}. \quad (\text{S30})$$

### D. Derivation of the trade-off relation on quantum time correlators in Eq. (2)

Starting from the general TUR on  $R(t)$  in Eq. (S30), we derive a trade-off relation beyond precision. Clearing the denominator of Eq. (S30) yields

$$|\langle \mathcal{F}_{\text{corr}} \rangle - \mathcal{C}_{\mathcal{F}_{\text{corr}}} | \leq \sqrt{\text{Var}[\mathcal{F}_{\text{corr}}] \mathcal{A}_{\mathcal{G}}}. \quad (\text{S31})$$

We proceed to evaluate the quantities in Eq. (S31). The observable  $\mathcal{F}_{\text{corr}}$  is defined as  $\mathcal{F}_{\text{corr}} = U_H^{(c)}(\sigma_x \otimes I_S)U_H^{(c)\dagger}$ , where the controlled unitary operation  $U_H^{(c)}$  is given by  $U_H^{(c)} = |0\rangle\langle 0| \otimes I + |1\rangle\langle 1| \otimes \mathcal{H}$ . Substituting this expression, we

obtain  $\mathcal{F}_{\text{corr}} = \sigma_x \otimes \mathcal{H}$ , with  $\mathcal{H}$  being unitary and Hermitian by definition. To emphasize the dependence on  $\mathcal{G}$  and  $\mathcal{H}$ , we introduce the inherent-dynamics contribution  $\mathcal{C}_{\mathcal{G}, \mathcal{H}}$ , which is equivalent to  $\mathcal{C}_{\mathcal{F}_{\text{corr}}}$ , as follows:

$$\mathcal{C}_{\mathcal{G}, \mathcal{H}} = \text{Re}[\text{Tr}[\rho_{S'S}^{V_0}(I_{S'} \otimes (V_0 V_0^\dagger)^{-1})(\sigma_x \otimes \mathcal{H})]]. \quad (\text{S32})$$

$\mathcal{C}_{\mathcal{G}, \mathcal{H}}$  is further calculated as

$$\begin{aligned} \mathcal{C}_{\mathcal{G}, \mathcal{H}} &= \text{Re}[\text{Tr}[\rho_{S'S}^{\mathcal{G}}(\sigma_x \otimes V_0^{-1} \mathcal{H} V_0)]] \\ &= \text{Re}[\text{Tr}[|+\rangle\langle+| \otimes \rho_S(0)(|0\rangle\langle 1| \otimes V_0^{-1} \mathcal{H} V_0 \mathcal{G} + |1\rangle\langle 0| \otimes \mathcal{G} V_0^{-1} \mathcal{H} V_0)]] \\ &= \text{Re}[\text{Tr}[\frac{1}{2}(|0\rangle\langle 1| + |1\rangle\langle 0|) \otimes \rho_S(0) V_0^{-1} \mathcal{H} V_0 \mathcal{G} + \frac{1}{2}(|0\rangle\langle 0| + |1\rangle\langle 1|) \otimes \rho_S(0) \mathcal{G} V_0^{-1} \mathcal{H} V_0]] \\ &= \frac{1}{2} \text{Re}[\text{Tr}[\rho_S(0)(V_0^{-1} \mathcal{H} V_0 \mathcal{G} + \mathcal{G} V_0^{-1} \mathcal{H} V_0)]] \\ &= \frac{1}{2} \text{Re}[\langle V_0^{-1} \mathcal{H} V_0 \mathcal{G} + \mathcal{G} V_0^{-1} \mathcal{H} V_0 \rangle] \end{aligned} \quad (\text{S33})$$

Next, the upper bound for the variance of  $\mathcal{F}_{\text{corr}}$  is calculated as

$$\text{Var}[\mathcal{F}_{\text{corr}}] = \langle \mathcal{F}_{\text{corr}}^2 \rangle - \langle \mathcal{F}_{\text{corr}} \rangle^2 \leq \langle \mathcal{F}_{\text{corr}}^2 \rangle = \langle \mathcal{F}_{\text{corr}}^\dagger \mathcal{F}_{\text{corr}} \rangle = 1. \quad (\text{S34})$$

Finally, by substituting Eqs. (S33) and (S34) and  $\langle \mathcal{F}_{\text{corr}} \rangle = \text{Re}[R(T)]$  into Eq. (S31), we obtain Eq. (2).

In the weak coupling limit where  $V_0^\dagger V_0$  satisfies  $V_0^\dagger V_0 = I_S - \epsilon$ , we performed a perturbative expansion of  $\mathcal{C}_{\mathcal{G}, \mathcal{H}}$  in the same way for  $\mathcal{C}_{\mathcal{F}_S}$ .  $\langle V_0^{-1} \mathcal{H} V_0 \mathcal{G} \rangle$  reads

$$\begin{aligned} \langle V_0^{-1} \mathcal{H} V_0 \mathcal{G} \rangle &\approx \left\langle (I - \frac{1}{2}\epsilon + \epsilon) U_0^\dagger \mathcal{H} V_0 \mathcal{G} \right\rangle \\ &= \langle V_0^\dagger \mathcal{H} V_0 \mathcal{G} \rangle + \langle \epsilon U_0^\dagger \mathcal{H} V_0 \mathcal{G} \rangle \\ &= \langle V_0^\dagger \mathcal{H} V_0 \mathcal{G} \rangle + \langle \epsilon U_0^\dagger \mathcal{H} U_0 \mathcal{G} \rangle. \end{aligned} \quad (\text{S35})$$

$\langle \mathcal{G} V_0^{-1} \mathcal{H} V_0 \rangle$  is similarly calculated as

$$\langle \mathcal{G} V_0^{-1} \mathcal{H} V_0 \rangle \approx \langle \mathcal{G} V_0^\dagger \mathcal{H} V_0 \rangle + \langle \mathcal{G} \epsilon U_0^\dagger \mathcal{H} U_0 \rangle. \quad (\text{S36})$$

Therefore,  $\mathcal{C}_{\mathcal{G}, \mathcal{H}}$  is approximated as

$$\mathcal{C}_{\mathcal{G}, \mathcal{H}} \approx \text{Re}[\langle \mathcal{G} V_0^\dagger \mathcal{H} V_0 \rangle] + \frac{1}{2} \text{Re}[\langle \epsilon U_0^\dagger \mathcal{H} U_0 \mathcal{G} \rangle + \langle \mathcal{G} \epsilon U_0^\dagger \mathcal{H} U_0 \rangle]. \quad (\text{S37})$$

The primary term is a time correlator regarding  $\mathcal{G}$  and  $\mathcal{H}$  when the system  $S$  is evolved by non-trace-preserving dynamics  $V_0$ .

### E. Circuits for $\mathcal{A}_{\mathcal{G}}$ and $\mathcal{C}_{\mathcal{F}_{\text{corr}}}$

We present the circuits used to measure the survival activity  $\mathcal{A}_{\mathcal{G}}$  and the inherent-dynamics contribution  $\mathcal{C}_{\mathcal{F}_{\text{corr}}}$ . To estimate  $\mathcal{A}_{\mathcal{G}}$ , we employ the approximation  $\mathcal{A}_{\mathcal{G}} \approx 1 - p_0$ , where  $p_0 = \text{Tr}[\rho_{S'S}^{\mathcal{G}} V_0^\dagger V_0]$ , obtained by truncating Eq. (S21) at  $N = 1$ . The probability  $p_0$  is estimated using the same circuit utilized to measure  $\text{Re}[R(T)]$ , as depicted in Fig. 1b, by measuring the environmental qubit  $E$ .

Measuring  $\mathcal{C}_{\mathcal{F}_{\text{corr}}} \approx 2C_1 - C_2$ , where  $C_1$  and  $C_2$  are defined in Eqs. (S26) and (S27), is the challenging part of this demonstration. As discussed in the section 1E,  $\mathcal{C}_{\mathcal{F}_{\text{corr}}}$  is determined through Hadamard tests for  $C_1$  and  $C_2$ . However, the straightforward implementation of these tests requires long circuits, which can be problematic. To mitigate this issue, we leverage the simplified form of  $\mathcal{C}_{\mathcal{F}}$  for  $\mathcal{F}_S$ , which includes  $\mathcal{F}_{\text{corr}}$ , as shown in Eq. (S16). This simplification allows us to avoid the use of controlled unitary operations involving three or more qubits. The circuit for measuring  $C_2$  is presented in Fig. S5, which, unlike the straightforward implementation in Fig. S2b, does not require a controlled  $U_{SE}$  operation. Furthermore, we employ the mid-circuit measurement for the environment, denoted by  $e_1$  in Fig. S5, which reduces the number of qubits needed and, consequently, the number of resource-intensive swap operations. We

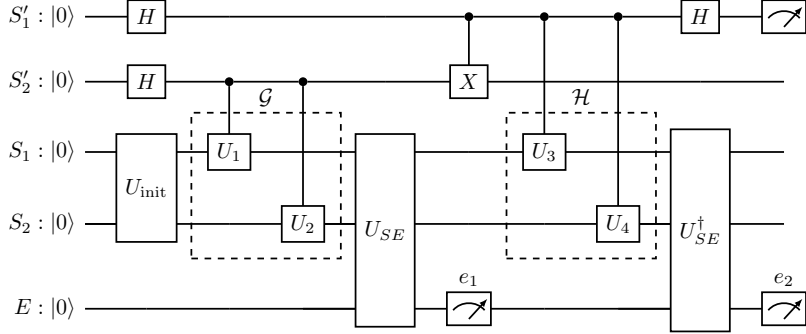


FIG. S5. Optimized circuit for measuring the  $C_2$  term in  $\mathcal{C}_{\mathcal{F}_{\text{corr}}}$ . The ancilla qubit  $S'_1$  is used to create the time correlator as shown in Fig. 1b, while the ancilla qubit  $S'_2$  is employed for the Hadamard test to measure the correlator in  $C_2$ . The circuit has the final measurement on  $S'_1$ , the mid-circuit measurement denoted by  $e_1$ , and the final measurement on the environment  $E$  denoted by  $e_2$ . The unitary operations  $U_i$  for  $i = 1, \dots, 4$  are determined by the specific choice of  $\mathcal{G}$  and  $\mathcal{H}$  operators.

remark that mid-circuit measurements take time to complete. However, in the circuit shown in Fig. S5, this is not an issue because the measurement can be performed concurrently with other operations involving  $S'_1$ ,  $S'_2$ ,  $S_1$ , and  $S_2$ . This is not the case for the straightforward circuit in Fig. S2b, where there is insufficient time for the mid-circuit measurement of the environment. A quantitative comparison of the depth of the straightforward and optimized circuits for  $C_2$  is provided in the next subsection. Remarkably, the same circuit used for measuring  $\text{Re}[R(T)]$ , shown in Fig. 1b, can also be used to measure  $C_1$  due to the simplified form of  $\mathcal{C}_{\mathcal{F}_{\text{corr}}}$ . In summary, we employ two circuits in this demonstration: one for measuring  $\text{Re}[R(T)]$ ,  $\mathcal{A}_{\mathcal{G}}$ , and  $C_1$ , as shown in Fig. 1b, and another for measuring  $C_2$ , as depicted in Fig. S5.

#### F. Circuit transpilation and depth evaluation

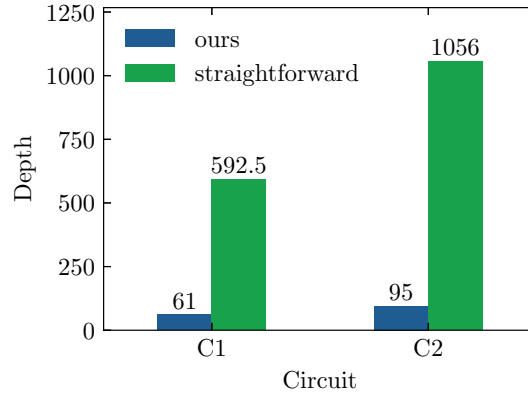


FIG. S6. Median depths of the transpiled circuits for measuring  $C_1$  and  $C_2$  in  $\mathcal{C}_{\mathcal{F}_{\text{corr}}}$ . The reported depths are based on 50 circuits, each corresponding to a different set of parameters.

The circuits designed thus far are logical circuits that ignore the physical constraints of qubits and operations. To execute these circuits on the quantum processor, they must be *transpiled* into physical circuits that satisfy these constraints. In this study, we use *Qiskit*, a standard Python library [13]. Specifically, we employ the *transpile* function with an *optimization\_level* of 3. This function performs stochastic optimization to reduce the depth of the circuits, although it is not powerful enough to generate our optimized (logical) circuit in Fig. S5 from the straightforward implementation in Fig. S2b.

Figure S6 shows the depths of the transpiled circuits for 50 sets of parameters described in the section III A. We observe a significant reduction in the depths achieved by our implementations for both  $C_1$  and  $C_2$ . The impact of the difference in depths on result accuracy is further evaluated in the demonstration of the equality condition of the general TUR, where the circuit depths are comparable to those in this demonstration.

### G. Empirical results

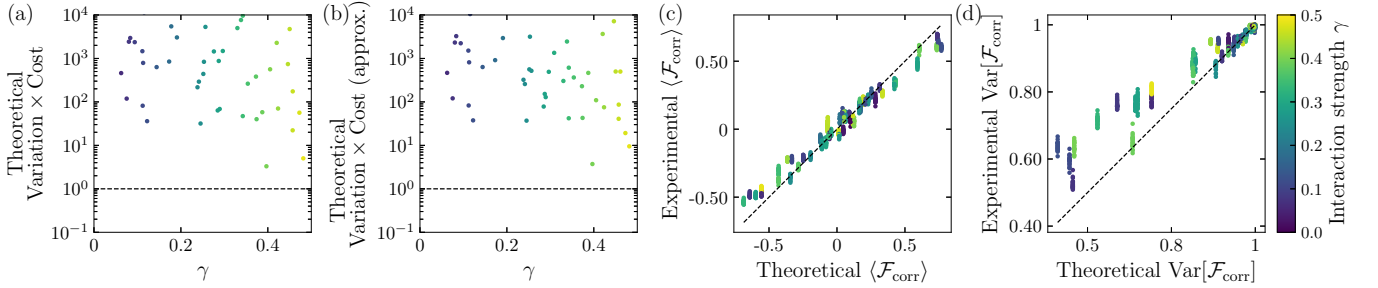


FIG. S7. Comparison of theoretical, approximated, and empirical values of  $\mathcal{F}_{\text{corr}}$ . (a) Theoretical product of the variation  $\text{Var}[\mathcal{F}_{\text{corr}}]/(\langle \mathcal{F}_{\text{corr}} \rangle - \mathcal{C}_{\mathcal{F}_{\text{corr}}})^2$  and the cost quantified by the survival activity  $\mathcal{A}_G$  plotted against  $\gamma$ . (b) Theoretically approximated product of variation and cost. (c) Theoretical and empirical values of  $\langle \mathcal{F}_{\text{corr}} \rangle$ . (d) Theoretical and empirical values of  $\text{Var}[\mathcal{F}_{\text{corr}}]$ . In (a) and (b), 50 data points are shown. In (c) and (d), the dashed line represents  $y = x$ , and  $50 \times 20$  data points are shown.

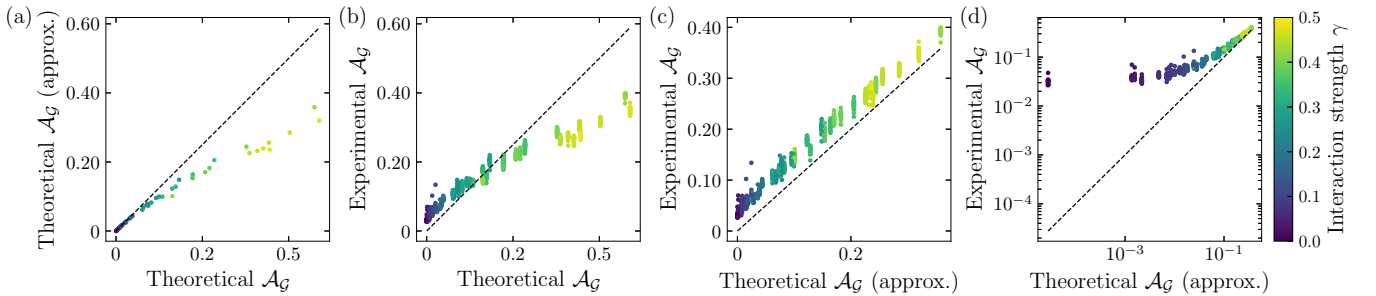


FIG. S8. Comparison of theoretical, approximated, and empirical values of the survival activity  $\mathcal{A}_G$ . (a) Theoretically approximated values plotted against theoretical values. (b) Empirical values plotted against theoretical values. (c) Empirical values plotted against theoretically approximated values. (d) Logarithmic plot of the data shown in (c). In panels (b)–(d), 50  $\times$  20 data points are displayed.

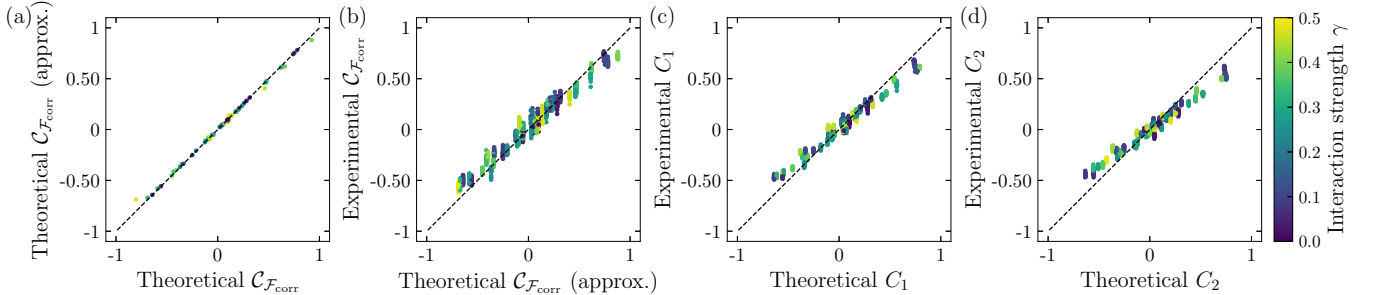


FIG. S9. Comparison of theoretical, approximated, and empirical values of  $\mathcal{C}_{\mathcal{F}_{\text{corr}}}$  and its component  $C_1$  and  $C_2$ . (a) Theoretically approximated values of  $\mathcal{C}_{\mathcal{F}_{\text{corr}}}$  plotted against theoretical values. (b) Empirical values of  $\mathcal{C}_{\mathcal{F}_{\text{corr}}}$  plotted against theoretically approximated values. (c) Empirical values of  $C_1$  plotted against theoretical values. (d) Empirical values of  $C_2$  plotted against theoretical values. In panels (b)–(d), 50  $\times$  20 data points are displayed.

We conducted demonstrations on 50 sets of parameter sets regarding  $\theta_i$  and  $\gamma$ , as described earlier in the section III A. For each set, we performed measurements on the corresponding circuits 4,000 times. To evaluate the fluctuation of the results, we repeated this procedure 20 times.

In Fig. S7, we show the influence of the theoretical approximation for  $\mathcal{A}_G$  and  $\mathcal{C}_{\mathcal{F}_{\text{corr}}}$ , as well as the empirical values of  $\langle \mathcal{F}_{\text{corr}} \rangle$  and  $\text{Var}[\mathcal{F}_{\text{corr}}]$ . First, from Figs. S7a and S7b, we observe that the influence of the theoretical approximation is not significant, which can be attributed to the small value of  $\gamma$ . We will later discuss the individual quantities

$\mathcal{A}_G$  and  $\mathcal{C}_{\mathcal{F}_{\text{corr}}}$ . From Fig. S7c, we find that the absolute values of  $\langle \mathcal{F}_{\text{corr}} \rangle$  are smaller than the predicted values for relatively large  $\gamma$ , although the empirical values show good agreement with the predictions. Considering that  $\langle \mathcal{F}_{\text{corr}} \rangle = \text{Re}[R(T)]$ , this trend is possibly due to unexpected noise that deteriorates the time correlators and that depolarizes the ancilla qubit. Finally, from Fig. S7d, we observe that the empirical values of  $\text{Var}[\mathcal{F}_{\text{corr}}]$  deviate from the predictions for small  $\text{Var}[\mathcal{F}_{\text{corr}}]$ . This is because  $\text{Var}[\mathcal{F}_{\text{corr}}]$  is given by  $\text{Var}[\mathcal{F}_{\text{corr}}] = 1 - \langle \mathcal{F}_{\text{corr}} \rangle^2$ , reflecting the deviation of  $\langle \mathcal{F}_{\text{corr}} \rangle$ .

Next, we present the results of the survival activity  $\mathcal{A}_G$  in Fig. S8. From Fig. S8a, we observe that the approximated values of  $\mathcal{A}_G$  are consistent with the exact values for small  $\gamma$ , but smaller than the theoretical values for relatively large  $\gamma$ . This is because the approximation  $\mathcal{A}_G \approx 1 - p_0$  is the first-order approximation of the survival activity. Furthermore, from Fig. S8b, we find that the empirical values of  $\mathcal{A}_G$  exhibit the same trend as the approximated theoretical values shown in Fig. S8a. Figure S8c shows a comparison of the empirical and approximated values. We observe that although the empirical values generally align well with the predictions, systematic deviations occur where the empirical values slightly exceed the predicted ones. This deviation is more clearly demonstrated in Fig. S8d, where the empirical values do not decrease as the predictions suggest.

Next, we present the results of the inherent-dynamics contribution  $\mathcal{C}_{\mathcal{F}_{\text{corr}}}$  in Fig. S9. From Fig. S9a, we observe that the approximated values of  $\mathcal{C}_{\mathcal{F}_{\text{corr}}}$  align well with the exact values. Furthermore, from Fig. S9b, we find that the empirical values of  $\mathcal{C}_{\mathcal{F}_{\text{corr}}}$  are also consistent with the predictions. From Figs. S9c and S9d, we observe that the absolute values of the empirical values of  $C_1$  and  $C_2$  are slightly smaller than the predicted values. Nevertheless, their empirical values align well with the predictions, highlighting the effectiveness of reducing the circuit depth. Note that the deviations of the empirical values of  $C_2$  from the predictions are slightly larger than those of  $C_1$ , probably due to differences in circuit depth.

#### IV. DEMONSTRATIONS ON THE EQUALITY CONDITION OF THE GENERAL TUR

##### A. Measurement of the optimal observable $\mathcal{F}_{\text{opt}}$

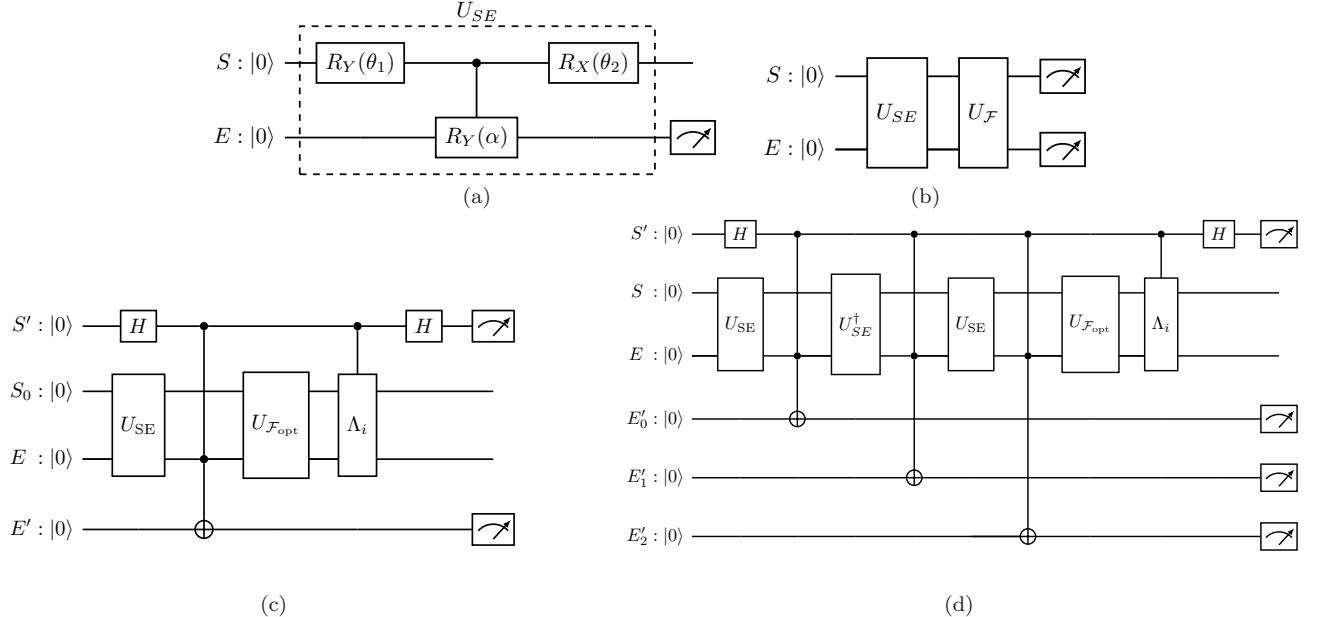


FIG. S10. Circuits for the optimal observable  $\mathcal{F}_{\text{opt}}$ , the unitary operation  $U_{SE}$  for a CPTP map, and the inherent-dynamics contribution  $\mathcal{C}_{\mathcal{F}_{\text{opt}}}$ . (a) Parameterized circuit for implementing  $U_{SE}$ . (b) Circuit for measuring  $\mathcal{F}_{\text{opt}}$ . (c) Optimized circuit for  $C_1$ . The controlled-CNOT gate, with control qubits denoted by black dots, is implemented using an approximate Toffoli gate. (d) Optimized circuit for  $C_2$ . Similar to (c), the controlled-CNOT gates are realized using approximate Toffoli gates.

As described in the derivation of the general TUR, equality is achieved for the observable  $\mathcal{F}_{\text{opt}} = \mathcal{L} = |\Psi_{SE}(T)\rangle\langle\Psi_{SE}(T)| - 1/2(|\tilde{\Psi}_{SE}(0)\rangle\langle\Psi_{SE}(T)| + |\Psi_{SE}(T)\rangle\langle\tilde{\Psi}_{SE}(0)|)$  when the initial state  $|\Psi_S(0)\rangle$  is pure. In this demonstration, we investigate a method to measure the statistics of this observable, given a simple unitary operator  $U_{SE}$ . Specifically, we consider a two-qubit system, with one qubit representing the principal system  $S$  and the other

representing the environment  $E$ , both of which are initialized in the  $|0\rangle$  state. The unitary operator  $U_{SE}$  is defined as illustrated in Fig. S10a and parameterized by random variables  $\theta_1$  and  $\theta_2$  sampled from  $[0, \pi/2]$ , and  $\alpha = \pi\gamma/2$ , consistent with our previous demonstrations for the time correlators. With these parameters, we can theoretically obtain  $\mathcal{L}$  and numerically diagonalize it as  $\mathcal{L} = U_{\mathcal{F}_{\text{opt}}}^\dagger \Lambda U_{\mathcal{F}_{\text{opt}}}$ , where  $U_{\mathcal{F}_{\text{opt}}}$  is the unitary matrix and  $\Lambda$  is the diagonal matrix. This form of  $\mathcal{L}$  can be interpreted as a Heisenberg picture of  $\Lambda$  under unitary dynamics with  $U_{\mathcal{F}_{\text{opt}}}$ . Consequently, we can access the statistics of  $\mathcal{L}$ , particularly its expectation and variance, by measuring  $\Lambda$  with separated measurements on  $S$  and  $E$ , as depicted in Fig. S10b. Thus, the survival activity can be measured using the circuit in Fig. S10a, while  $\langle \mathcal{L} \rangle$  and  $\text{Var}[\mathcal{L}]$  can be obtained using the circuit in Fig. S10b.

### B. Circuits for $\mathcal{C}_{\mathcal{F}_{\text{opt}}}$

Measurement of the inherent-dynamics contribution  $\mathcal{C}_{\mathcal{F}}$  is based on Hadamard tests, as described in the section IE. One notable difference between the circuits for  $\mathcal{C}_{\mathcal{F}_{\text{opt}}}$  and general  $\mathcal{C}_{\mathcal{F}}$  is the inclusion of the operation  $U_{\mathcal{F}_{\text{opt}}}$  followed by controlled  $\Lambda_i$  in the former. Here,  $\Lambda_i$ 's are Hermitian and unitary operators satisfying  $\Lambda = \sum_i \Lambda_i$ . Consequently, to obtain the value for  $\Lambda$ , we must execute circuits corresponding to each  $\Lambda_i$  and sum the resulting values. Interestingly, we observe that for all the investigated circuits,  $\Lambda$  can be empirically expressed in the form  $\Lambda = c(|00\rangle\langle 00| - |11\rangle\langle 11|)$ , where  $c$  is a scalar dependent on each  $U_{SE}$ . This peculiarity may be attributed to the structure of the  $U_{SE}$  circuit depicted in Fig. S10a. As a result of this property, we only need to implement circuits for  $\Lambda_1 = \sigma_z \otimes I_E$  and  $\Lambda_2 = I_S \otimes \sigma_z$ .

The measurement of  $\mathcal{C}_{\mathcal{F}}$  presents a significant challenge in this demonstration. The straightforward implementation of the Hadamard test for  $C_1$  and  $C_2$ , as described in the section IE, necessitates lengthy circuits due to the repeated application of controlled  $U_{SE}$  and controlled  $U_{\mathcal{F}_{\text{opt}}}$ . To address this challenge, we leverage the relationship between  $U_{SE}$  and  $V_0$ . As illustrated in Fig. S10c for  $C_1$ , we can implement the control unitary operation that applies  $U_{SE}$  to the composite system  $S+E$  when  $S'$  is in  $|0\rangle$  and  $V_0$  to  $S$  when  $S'$  is in  $|1\rangle$  using a controlled-CNOT gate, also known as a Toffoli gate. This approach also eliminates the need to apply the controlled  $U_{\mathcal{F}_{\text{opt}}}$ . Furthermore, we can reduce the number of CNOT gates required for the Toffoli gate by employing an approximate Toffoli gate [14]. The approximate Toffoli gate behaves identically to the exact Toffoli gate, except for a few specific inputs. By allowing such errors, the approximate Toffoli gate requires only three CNOT gates, unlike the six CNOT gates needed for the exact Toffoli gate (note that these numbers refer to logical circuits). Remarkably, the approximate Toffoli gate behaves *exactly* when the target is in  $|0\rangle$ , which is the case in our setup. Figure S10d depicts the circuit for  $C_2$ , which also benefits from the circumvention of controlled unitary operations and the introduction of approximate Toffoli gates. The effectiveness of this approach in reducing circuit depth is quantitatively evaluated in the next subsection.

### C. Depth evaluation

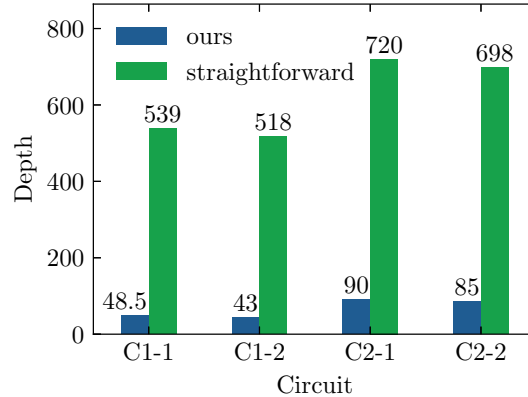


FIG. S11. Depths of transpiled circuits for  $C_1$  and  $C_2$  regarding  $\mathcal{F}_{\text{opt}}$ . The median depths of 50 circuits, corresponding to 50 different sets of parameters, are presented. The notation  $C_j-i$  denotes the circuit for  $C_j$  associated with  $\Lambda_i$ .

Similar to the previous demonstration for  $R(T)$ , we conduct demonstrations on 50 sets of parameters for  $U_{\text{init}}$  and  $U_{SE}$ . Figure S11 shows the depths of the transpiled circuits for  $C_1$  and  $C_2$  for these setups. While slight differences

exist between the circuits for  $\Lambda_1$  and  $\Lambda_2$ , our approach markedly reduces the overall depth. The effectiveness of this depth reduction on empirical result accuracy is demonstrated in Fig. 2.

#### D. Empirical results

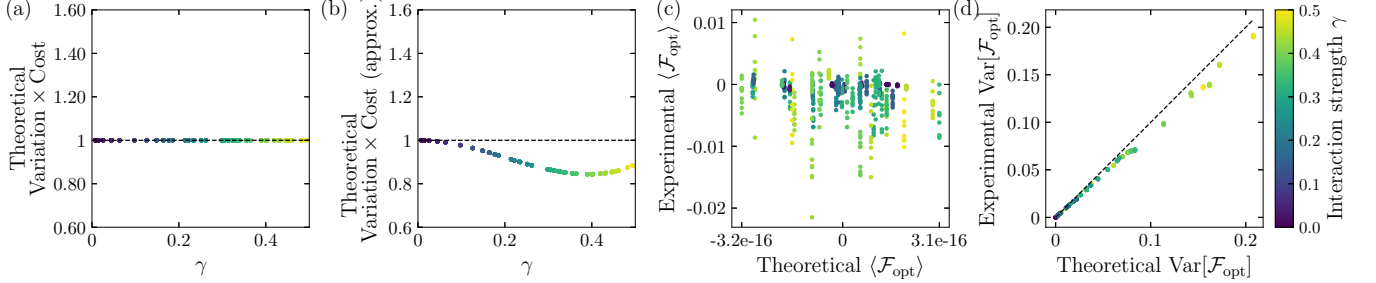


FIG. S12. Comparison of the theoretical, approximated, and empirically obtained values regarding  $\mathcal{F}_{\text{opt}}$ . The interaction strength  $\gamma$  is represented by different colors. (a) Theoretical values of the product of the variation  $\text{Var}[\mathcal{F}_{\text{opt}}]/(\langle \mathcal{F}_{\text{opt}} \rangle - \mathcal{C}_{\mathcal{F}_{\text{opt}}}^2)$  and the cost quantified by the survival activity  $\mathcal{A}$ , plotted against  $\gamma$ . (b) Theoretically approximated values of the product of variation and cost. (c) Comparison of the theoretical and empirical values of the expectation value  $\langle \mathcal{F}_{\text{opt}} \rangle$ . (d) Comparison of the theoretical and empirical values of the variance  $\text{Var}[\mathcal{F}_{\text{opt}}]$ . In (c) and (d),  $50 \times 10$  data points are plotted.

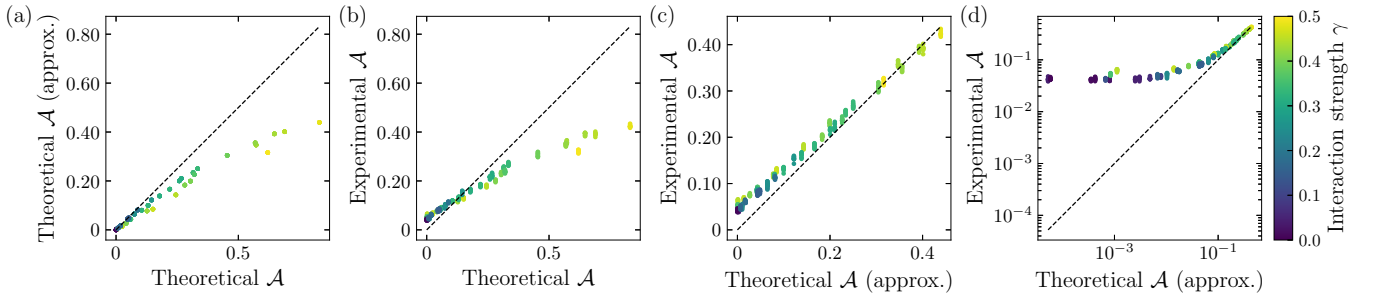


FIG. S13. Comparison of theoretical, approximated, and empirical values of  $\mathcal{A}$ . (a) Theoretically approximated values plotted against theoretical values. (b) Empirical values plotted against theoretical values. (c) Empirical values plotted against theoretically approximated values. (d) Logarithmic plot of the data presented in (c). For panels (b)–(d),  $50 \times 10$  data points are displayed.

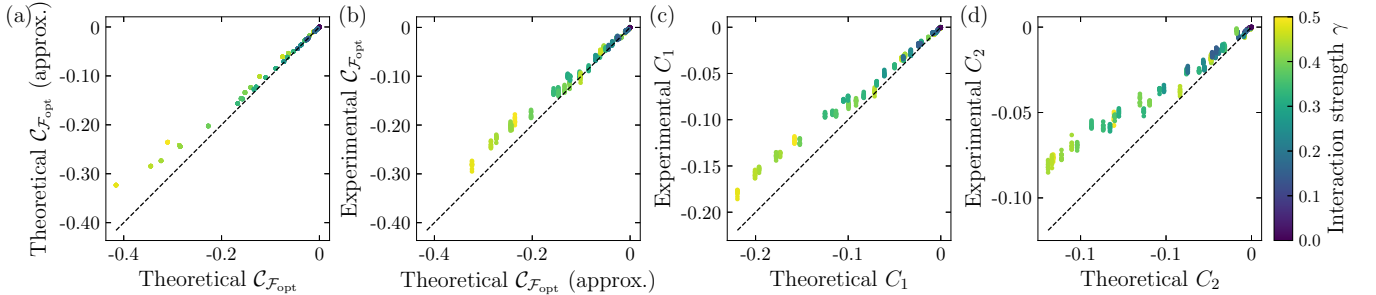


FIG. S14. Comparison of theoretical, approximated, and empirical values of  $\mathcal{C}_{\mathcal{F}_{\text{opt}}}$ . (a) Theoretically approximated values of  $\mathcal{C}_{\mathcal{F}_{\text{opt}}}$  plotted against theoretical values. (b) Empirical values of  $\mathcal{C}_{\mathcal{F}_{\text{opt}}}$  plotted against theoretically approximated values. (c) Empirical values of  $C_1$  plotted against theoretical values. (d) Empirical values of  $C_2$  plotted against theoretical values. For panels (b)–(d),  $50 \times 10$  data points are displayed.

We conducted demonstrations on 50 sets of parameter combinations for  $\theta_i$  and  $\gamma$ . For each combination, we

performed 8,000 measurements on the corresponding circuits. This procedure was repeated 10 times for the Heron processor and 5 times for the Eagle processor, which is described later.

Figure S12 shows the influence of the theoretical approximation of  $\mathcal{A}$  and  $\mathcal{C}_F$ , as well as the empirical values of  $\langle \mathcal{F}_{\text{opt}} \rangle$  and  $\text{Var}[\mathcal{F}_{\text{opt}}]$ . As shown in Fig. S12a, our design of  $\mathcal{F}_{\text{opt}}$  achieves equality in the general TUR. The influence of the theoretical approximation is depicted in Fig. S12b, where the product of variation and  $\mathcal{A}$  falls below one, particularly for relatively large  $\gamma$  values. We consider the deviation to be insignificant compared to the fluctuation of the empirical values, as demonstrated in Fig. 2. Furthermore, Fig. S12c reveals that the empirical values of  $\langle \mathcal{F}_{\text{opt}} \rangle$  are nearly zero, aligning with the theoretical prediction of  $\langle \mathcal{F}_{\text{opt}} \rangle = 0$ . The variance of  $\mathcal{F}_{\text{opt}}$  is presented in Fig. S12d, where the empirical values exhibit strong agreement with the predictions.

Figure S13 presents the results of the survival activity  $\mathcal{A}$ . As seen in Fig. S13a, which is similar to Fig. S8a for the previous demonstrations, the approximated values of  $\mathcal{A}$  align with the exact values for small  $\gamma$  but are smaller than the exact values for relatively large  $\gamma$ . Figure S13b reveals that the empirical values of  $\mathcal{A}$  follow the same trend as the approximated theoretical values in Fig. S13a. However, we observe that the empirical values slightly surpass the predictions for small  $\gamma$ , which is more clearly illustrated in Figs. S13c and S13d. We attribute the deviation of the empirical values of the product of variation and cost from the limit in Fig. 2c to this discrepancy. The order of the empirical values of  $\mathcal{A}$  for small  $\gamma$  is  $10^{-2}$ , which coincides with that of the readout error ( $1.95 \times 10^{-2}$ ).

Figure S14 presents the results of the inherent-dynamics contribution  $\mathcal{C}_{\mathcal{F}_{\text{opt}}}$ . As shown in Fig. S14a, the approximated values of  $\mathcal{C}_{\mathcal{F}_{\text{opt}}}$  are slightly exceed the theoretical values for large  $\gamma$ . This trend is mirrored by the empirical values in Figs. S14b, S14c, and S14d.

### E. Comparison to the straightforward implementation for $\mathcal{C}_F$

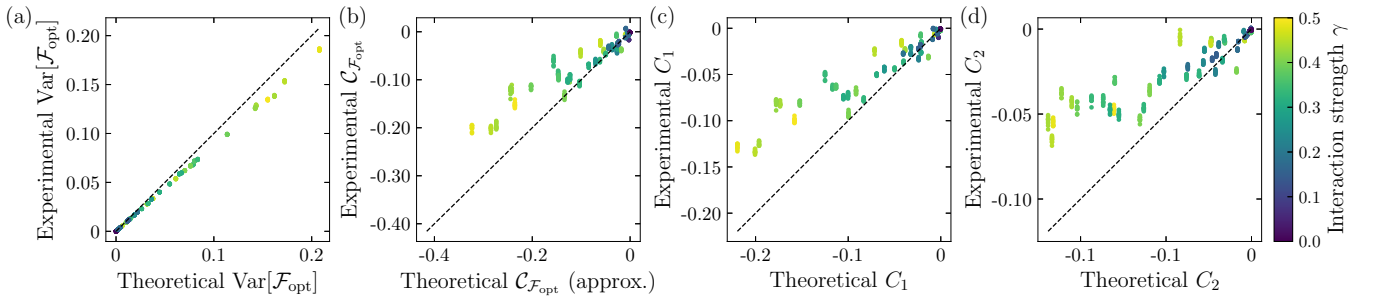


FIG. S15. Comparison of theoretical, approximated, and empirical results regarding  $\mathcal{F}_{\text{opt}}$  using the straightforward implementation. (a) Empirical values of  $\text{Var}[\mathcal{F}_{\text{opt}}]$  plotted against theoretical values. (b) Empirical values of  $\mathcal{C}_{\mathcal{F}_{\text{opt}}}$  plotted against theoretically approximated values. (c) Empirical values of  $C_1$  plotted against theoretical values. (d) Empirical values of  $C_2$  plotted against theoretical values. For panels (b)–(d),  $50 \times 10$  data points are displayed.

In Fig. S15, we present the results of the straightforward implementation of the Hadamard test for  $\mathcal{C}_F$ . Fig. S15a, which displays  $\text{Var}[\mathcal{F}_{\text{opt}}]$ , confirms that the qubit and gate quality for this demonstration is comparable to that of the previous demonstrations. However, Fig. S15b reveals that the empirical values of  $\mathcal{C}_{\mathcal{F}_{\text{opt}}}$  are noisy and scattered compared to the predicted values. This discrepancy can be attributed to the fact that the straightforward implementation requires circuits with approximately ten times the depth of the optimized circuits, leading to increased noise susceptibility. Figures S15c and S15d illustrate that  $C_2$ , which requires longer circuits than  $C_1$ , is more severely affected by noise. These findings stand in sharp contrast to the results obtained using the optimized circuits, as shown in Fig. S14.

### F. Comparison to the Eagle processor

To compare the empirical results on the equality condition of the general TUR across different quantum processors, we conducted the same demonstrations using the Eagle processor. Figure S16 presents the results of these demonstrations. As shown in Fig. S16a, the empirical values violate the general TUR. Figure S16b reveals that the empirical values of  $\text{Var}[\mathcal{F}_{\text{opt}}]$  align well with the predictions, and the difference between the processors is not apparent. However, Figs. S16c and S16d demonstrate that the empirical values of  $C_1$  and  $C_2$  on the Eagle processor are significantly noisier

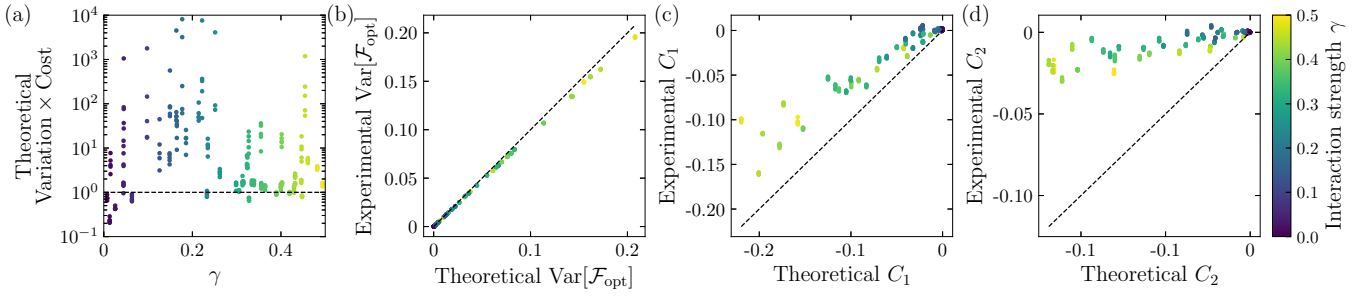


FIG. S16. Results on  $\mathcal{F}_{\text{opt}}$  obtained with the Eagle processor. (a) Empirical values of the product of the variance and cost plotted against the interaction strength  $\gamma$ . (b) Empirical values of  $\text{Var}[\mathcal{F}_{\text{opt}}]$  plotted against theoretical values. (c) Empirical values of  $C_1$  plotted against theoretical values. (d) Empirical values of  $C_2$  plotted against theoretical values. For all panels,  $50 \times 5$  data points are displayed.

and deviate from the predictions. These findings suggest that the difference in processor accuracy plays a crucial role in demonstrations involving the general TUR, particularly when investigating its equality condition.

---

[1] Y. Hasegawa, Thermodynamic uncertainty relation for general open quantum systems, *Phys. Rev. Lett.* **126**, 010602 (2021).

[2] M. Hotta and M. Ozawa, Quantum estimation by local observables, *Phys. Rev. A* **70**, 022327 (2004).

[3] B. M. Escher, R. L. de Matos Filho, and L. Davidovich, General framework for estimating the ultimate precision limit in noisy quantum-enhanced metrology, *Nat. Phys.* **7**, 406 (2011).

[4] R. Somma, G. Ortiz, J. E. Gubernatis, E. Knill, and R. Laflamme, Simulating physical phenomena by quantum networks, *Phys. Rev. A* **65**, 042323 (2002).

[5] IBM, IBM Quantum, <https://quantum.ibm.com/>, accessed: 2024-4-25.

[6] IBM, IBM debuts next-generation quantum processor & IBM Quantum System Two, extends roadmap to advance era of quantum utility, <https://newsroom.ibm.com/2023-12-04-IBM-Debuts-Next-Generation-Quantum-Processor-IBM-Quantum-System-Two>, accessed: 2024-4-29.

[7] J. Koch, T. M. Yu, J. Gambetta, A. A. Houck, D. I. Schuster, J. Majer, A. Blais, M. H. Devoret, S. M. Girvin, and R. J. Schoelkopf, Charge-insensitive qubit design derived from the Cooper pair box, *Phys. Rev. A* **76**, 042319 (2007).

[8] For each metric, the median value across all qubits or gates was calculated for each day. The mean and standard deviation of these daily medians were then computed for the month, considering only days with available data from Ref. [5]. The metrics for CZ error and ECR error (for the Eagle processor) represent the average gate fidelity over all possible inputs.

[9] IBM, IBM Quantum breaks the 100-qubit processor barrier, <https://www.ibm.com/quantum/blog/127-qubit-quantum-processor-eagle>, accessed: 2024-2-24.

[10] N. Sundaresan, I. Lauer, E. Pritchett, E. Magesan, P. Jurcevic, and J. M. Gambetta, Reducing unitary and spectator errors in cross resonance with optimized rotary echoes, *PRX Quantum* **1**, 020318 (2020).

[11] D. C. McKay, I. Hincks, E. J. Pritchett, M. Carroll, L. C. G. Govia, and S. T. Merkel, Benchmarking quantum processor performance at scale, [arXiv:2311.05933](https://arxiv.org/abs/2311.05933) (2023).

[12] J. S. Pedernales, R. Di Candia, I. L. Egusquiza, J. Casanova, and E. Solano, Efficient quantum algorithm for computing n-time correlation functions, *Phys. Rev. Lett.* **113**, 020505 (2014).

[13] Qiskit contributors, Qiskit, <https://github.com/QISKit>, accessed: 2024-6-2.

[14] Y. He, M.-X. Luo, E. Zhang, H.-K. Wang, and X.-F. Wang, Decompositions of n-qubit Toffoli gates with linear circuit complexity, *Int. J. Theor. Phys.* **56**, 2350 (2017).